

# Magnetomechanical characterization and unified energy model for the quasistatic behavior of ferromagnetic shape memory Ni–Mn–Ga\*

Neelesh N Sarawate<sup>1,3</sup> and Marcelo J Dapino<sup>2</sup>

<sup>1</sup> GE Global Research Center, 1 Research Circle, Niskayuna, NY 12309, USA

<sup>2</sup> Department of Mechanical Engineering, The Ohio State University, Columbus, OH 43210, USA

E-mail: [sarawate@ge.com](mailto:sarawate@ge.com) and [dapino.1@osu.edu](mailto:dapino.1@osu.edu)

Received 5 July 2009, in final form 11 December 2009

Published 22 January 2010

Online at [stacks.iop.org/SMS/19/035001](http://stacks.iop.org/SMS/19/035001)

## Abstract

This paper presents an overview of the characterization and modeling of single crystal ferromagnetic shape memory Ni–Mn–Ga. A continuum thermodynamics model is presented which describes the magnetomechanical characterization of single crystal Ni–Mn–Ga for the following behavior: (i) sensing effect; (ii) actuation effect; (iii) blocked force (stress generation). The thermodynamic potentials, namely the magnetic Gibbs energy and the Gibbs energy, are obtained from the Helmholtz energy in order to arrive at the set of required independent and dependent variables; the potentials include magnetic energy consisting of Zeeman, magnetostatic and anisotropy components, and mechanical energy consisting of elastic and twinning components. Mechanical dissipation and the microstructure of Ni–Mn–Ga are incorporated in the continuum model through the internal state variables volume fraction, domain fraction, and magnetization rotation angle. The constitutive response of the material is obtained by restricting the process through the second law of thermodynamics. The model requires only seven parameters identified from two simple experiments. Several interesting characteristics of Ni–Mn–Ga are examined in concert with the magnetomechanical characterization.

(Some figures in this article are in colour only in the electronic version)

## 1. Introduction

Ferromagnetic shape memory alloys (FSMAs) in the Ni–Mn–Ga system are a class of active materials which typically generate 6% strain in response to externally applied magnetic fields [1]. In contrast to conventional heat driven shape memory alloys (SMAs), the magnetically driven FSMAs exhibit high operating frequency in the kHz range [2, 3], making them attractive for actuation applications. Most of the work on characterization and modeling of FSMAs has been focused on quasistatic actuation, i.e., strain dependence on magnetic field (e.g. see review papers [4, 5]). The sensing

effect, i.e., magnetization dependence on external strain input was recently characterized [6] and modeled [7] using continuum thermodynamics principles. This work extends the model to incorporate actuation and blocked force behavior. The model uses a unified continuum thermodynamics framework to describe the following magnetomechanical interdependencies: (i) stress and magnetization dependence on strain input at varied bias fields (sensing), (ii) strain and magnetization dependence on field input at varied bias stresses (actuation), (iii) stress and magnetization dependence on field input at varied bias blocked strains (blocked force).

The strain mechanism in FSMAs is well established in the literature [8–10]. In the low temperature martensite phase, FSMAs consist of a self-accommodating twin-variant

\* This work was performed by the authors at The Ohio State University.

<sup>3</sup> Author to whom any correspondence should be addressed.

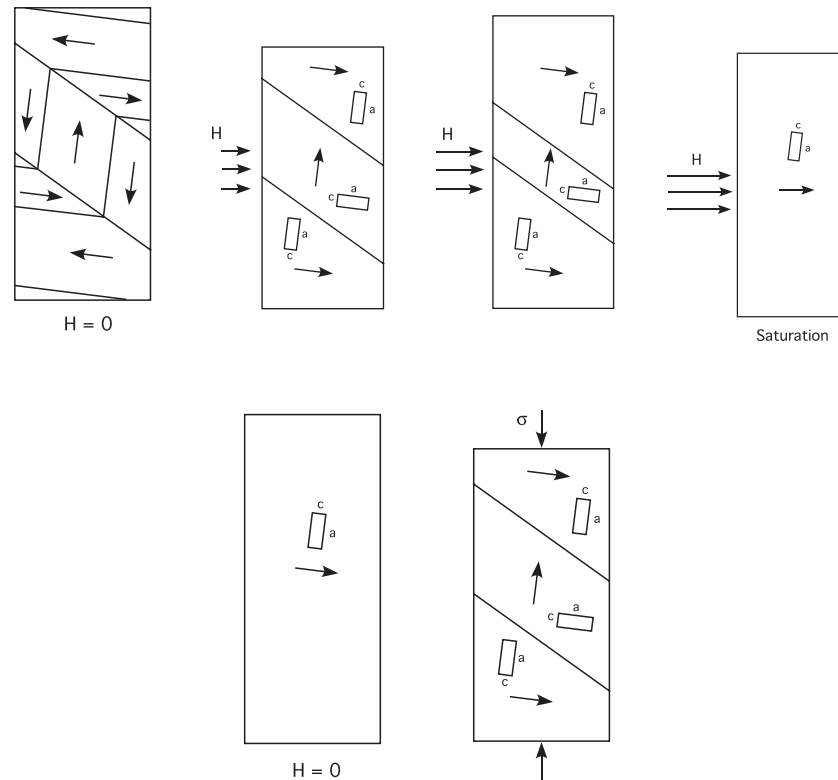


**Figure 1.** Schematic of strain mechanism in FSMA under transverse field and longitudinal stress.

structure consisting of crystals with orthogonal orientations of magnetically easy  $c$ -axes, separated by a twin boundary as shown in figure 1. The twin-variant rearrangement or twin boundary motion results in deformation of the material due to reorientation of the crystal structure. The twin boundary can be driven by externally applied transverse magnetic fields, or by longitudinal compressive stress. A magnetic field applied in the  $x$  direction produces alignment of the magnetization vectors and the crystal  $c$ -axis along the field direction, thereby producing positive strain in the  $y$  direction. A compressive stress in the  $y$  direction produces alignment of the  $c$ -axis and magnetization vectors along the  $y$  direction, thus restoring the initial configuration. The maximum possible strain depends on the crystal geometry, with a typical value of 6% in commercially available single crystal specimen [11].

Several models have been proposed for describing twin-variant rearrangement in FSMA, with the primary intent of characterizing the magnetic field induced strain or actuator behavior. The most common approach relies on construction and minimization of an energy function to obtain stress, strain, and magnetization responses to magnetic fields.

James and Wuttig [12] presented a model based on a constrained theory of micromagnetics (see also [13, 14]). The terms contributing to the free energy in their model are the Zeeman energy, the magnetostatic energy and the elastic energy. The magnetization of Ni–Mn–Ga is assumed to be fixed to the magnetic easy axis of each martensitic variant because of the material's high magnetic anisotropy. The microstructural deformations and the resulting macroscopic strain and magnetization response are predicted

by detecting low-energy paths between initial and final configurations. They conclude that the typical strains observed in martensite, together with the typical easy axes observed in ferromagnetic materials, lead to layered domain structures that are simultaneously mechanically and magnetically compatible. Because of the complexity of the model, it has been implemented only for certain simplified cases [15, 16].

After the discovery of Ni–Mn–Ga, Likhachev and Ullakko proposed a model that has become the basis for much of the subsequent modeling work [9, 17–22]. In this model, the anisotropy energy difference between the two variants is identified as the chief driving force. The derivative of the easy-axis and hard-axis magnetic energy difference is defined as the magnetic field induced driving force acting on a twin boundary. The magnetization is assumed to be a linear combination of easy-axis and hard-axis magnetization values related by the volume fraction. It is argued that regardless of the physical nature of the driving force, twin boundary motion should be initiated at equivalent load levels. The strain output for a given magnetic field input can be predicted through an analytical interpolation of mechanical stress–strain experimental data by replacing the mechanical stress with an effective force due to the field. A similar model was utilized by Straka and Heczko [23–25] for describing the stress–strain response at varied bias fields.

O'Handley [8] presented a model that quantifies the strain and magnetization dependence on field by energy minimization. The Zeeman energy difference ( $\Delta \mathbf{M} \cdot \mathbf{H}$ ) across the twin boundary is the driving force responsible for strain generation. The contributions of elastic, Zeeman,

and anisotropy energy are considered, with the latter defining three cases depending on its strength being low, medium, or high. This model is anhysteretic because technique of energy minimization results in thermodynamically reversible behavior. For the intermediate anisotropy case, a parametric study was conducted which shows the influence of varying elastic and magnetic anisotropy energies. This work provided a significant advancement towards modeling of FSMAs by proposing the twin boundary mechanism due to the interaction between anisotropy and Zeeman energy as the reason behind stress generation. Further work by the authors has been based on this model, with focus on modeling the strain–field behavior from micromagnetic considerations [26–28].

A model by Couch and Chopra [29–31] is based on an approach similar to that by Brinson [32, 33] for thermal shape memory materials. The stress is assumed to be a linear combination of strains, volume fractions and magnetic fields. The model was developed to describe the stress–strain behavior at varied magnetic fields and quantify the transition from irreversible to reversible behavior. The model parameters are obtained as for thermal shape memory alloys, by using the values of slopes that the curves of critical stress values make when plotted against the bias magnetic field. The critical stresses are expressed as a function of the magnetic field using these slopes. While this model is tractable, the identification of model parameters requires stress–strain testing over a range of bias fields in order to obtain the necessary stress profiles as a function of field.

Glavatska *et al* [34] developed a statistical model for magnetic field induced strain by relating the magnetoelastic interactions to the internal microstress in the martensite. The probability of rearrangement for the twins in which the stresses are near the critical values is described through a statistical distribution. Chernenko *et al* [35, 36] further modified this model to describe the quasiplastic and superelastic stress–strain response of FSMAs at varied bias fields.

A thermodynamic approach was introduced by Hirsinger and LExcellent, and was used in their subsequent publications [37, 10, 38–40]. Magnetomechanical energy expressions were developed. The microstructure of single crystal Ni–Mn–Ga was represented by internal state variables; the evolution of these variables was used to quantify the strain and magnetization response to applied magnetic fields. The anisotropy energy effect was not considered in [10] but was later considered in [38, 41] in order to model the magnetization.

Kiefer and Lagoudas [42–44] employed a similar approach with a more systematic thermodynamics treatment. Polynomial and trigonometric hardening functions were introduced to account for interaction of evolving volume fractions. However, this leads to increased number of model parameters. Faidley *et al* [45–47] used the thermodynamic approach to describe reversible magnetic field induced strain in research-grade Ni–Mn–Ga. The Gibbs energy potential was constructed for the case when the twin boundaries are pinned by dislocations, which had been previously shown by Malla *et al* [48] to allow in some cases for reversible twin boundary bowing when the single crystal is driven with a

collinear magnetic field and stress pair. While similar in concept to the models by Hirsinger and LExcellent [10] and Kiefer and Lagoudas [42], in this model the energy of a mechanical spring is added to the Zeeman and elastic energies to account for the internal restoring force supplied by the pinning sites. The anisotropy energy was assumed to be infinite in [42] and [45] and magnetostatic energy was not considered with the argument that it depends on the geometry of a sample. One tenet of the proposed model is that the magnetostatic energy is an important component of the magnetization response, which is critical for describing the sensing effect. The magnetostatic energy is thus considered as a means to quantify the demagnetization field. While the magnitude of the demagnetization field depends on a specimen's shape, it can be assumed to be uniform throughout a continuum.

In this paper, a thermodynamic model is presented to describe the sensing behavior. The focus is on modeling the magnetization versus strain behavior and magnetic field induced pseudoelasticity in Ni–Mn–Ga FSMAs. Further, this sensing model is extended to describe the actuation and blocked force behavior of single crystal Ni–Mn–Ga.

We present a unified magnetomechanical model based on a continuum thermodynamics approach similar to that in [10, 42, 45]. However, the primary intent is to present an improved sensing effect model as compared to [7]; which is then extended to model the actuation and blocked force behavior. Numerous magnetomechanical characterization factors like the flux density sensitivity with respect to strain, the magnetic field induced stress, the maximum field induced strain and optimum bias stress, the variation of initial susceptibility with blocked strain and the maximum generated blocked stress are presented in terms of both experimental results and model at various stages in the paper, illustrating the rich magnetomechanical coupling in Ni–Mn–Ga. This coupling, however, should not be viewed in the traditional sense of the magnetostrictive effect. The magnetomechanical coupling in Ni–Mn–Ga results from the competition between the strong magnetocrystalline anisotropy and Zeeman energy due to applied fields. The conventional magnetoelastic coupling resulting from magnetostriction, or domain rotation, is often ignored in modeling of Ni–Mn–Ga as the associated deformations are several orders of magnitude larger than the associated magnetostrictive strains [49, 50]. This coupling must be included for modeling the blocked force behavior when the material is constrained from mechanical deformation. The experimental characterization of sensing and blocked force is explained briefly. The experimental data on actuation is obtained from [51], as actuation characterization is well established.

The outline of the paper is as follows. A brief thermodynamic background with the inclusion of magnetic terms is given in section 2. The incorporation of the microstructure in the continuum thermodynamics framework using the internal state variables volume fraction, domain fraction, and magnetization rotation angle is discussed in section 3. Sections 4–7 discuss the sensing model, which includes magnetic and mechanical energy formulations (4) followed by the discussion of evolution of internal state variables

(sections 5 and 6) and model results (section 7). A specific form of thermodynamic potential termed magnetic Gibbs energy is defined which includes Zeeman, magnetostatic, and anisotropy energy contributions. The mechanical energy includes an elastic component and dissipative effects due to twinning. As is often done for modeling of shape memory alloys, the total strain is decomposed into an elastic and twinning strain. The process associated with magnetization variables is assumed to be reversible but the evolution of volume fraction is assumed to be dissipative, which implies that the constitutive response depends on the volume fraction history. The model is extended to the actuation effect in section 8 to describe strain dependence on field. Section 9 presents the characterization and modeling of blocked (zero strain) force, and the concluding remarks are presented in section 10. The model requires only seven parameters, which are determined through the following simple experiments: stress–strain curve at zero bias field, and easy-axis and hard-axis magnetization curves, with one additional parameter for the blocked force model. The comparison of model results with experimental measurements is presented throughout the paper.

## 2. Thermodynamic framework

The first law of thermodynamics dictates that the rate of change of internal energy of any part  $S$  of a body is equal to the rate of mechanical work of the net external force acting on  $S$  plus all other energies that enter or leave  $S$ . For solids, the Lagrangian or referential form is used, where the reference (unloaded) configuration is known. For a thermo-magnetomechanical solid, the conservation law is given in local form as,

$$\rho \dot{\epsilon} = \mathbf{P} \cdot \dot{\mathbf{F}} + \mu_0 \vec{\mathbf{H}} \cdot \dot{\vec{\mathbf{M}}} + \rho r - \text{Div } \mathbf{q}, \quad (1)$$

where  $\epsilon$  is the specific internal energy,  $\rho$  is the density of the material in referential coordinates,  $\mathbf{P}$  is the first Piola–Kirchhoff stress tensor,  $\mathbf{F}$  is the deformation gradient tensor,  $r$  is the specific heat source inside the system and  $\mathbf{q}$  is a referential heat flux vector representing the heat going out of the system. The term  $\mathbf{P} \cdot \dot{\mathbf{F}}$  represents the stress power, or the rate of work done on the system by external mechanical action. The term  $\mu_0 \vec{\mathbf{H}} \cdot \dot{\vec{\mathbf{M}}}$  represents the energy supplied to the material by a magnetic field [52], with  $\vec{\mathbf{H}}$  denoting the resultant applied magnetic field vector and  $\vec{\mathbf{M}}$  the net magnetization vector inside the material. The first law assumes that mechanical energy can be converted to heat energy and vice versa with no restrictions placed on the transformation. In actuality, the inverse transformation is subject to definite restrictions which are formalized through the second law of thermodynamics.

One mathematical representation of the second law is the Clausius–Duhem inequality, which states that the rate of change of entropy of part  $S$  at time  $t$  is greater than or equal to the entropy increase rate due to the specific heat supply rate  $r$  minus the entropy decrease rate due to the heat flux rate. Mathematically, this is expressed in local form as,

$$\rho \dot{\eta} \geq \rho \frac{r}{\Theta} - \text{Div} \left( \frac{\mathbf{q}}{\Theta} \right), \quad (2)$$

where  $\Theta$  is the absolute temperature, and  $\eta$  is the specific entropy. In short, the Clausius–Duhem inequality states that mechanical forces and deformation can only increase the entropy of a part  $S$  of the body.

Elimination of  $r$  from (1) and (2) gives

$$\rho \Theta \dot{\eta} - \rho \dot{\epsilon} + \mathbf{P} \cdot \dot{\mathbf{F}} + \mu_0 \vec{\mathbf{H}} \cdot \dot{\vec{\mathbf{M}}} - \frac{1}{\Theta} \mathbf{q} \cdot \text{Grad } \Theta \geq 0. \quad (3)$$

In the case of the sensing behavior, the material is subjected to a uniaxial strain ( $\epsilon$ ) along the  $y$ -direction in presence of magnetic field ( $H$ ) along the transverse  $x$ -direction. This results in the generation of engineering stress ( $\sigma$ ) along the  $y$ -direction and magnetization ( $M$ ) along the  $x$ -direction. Therefore, expression (3) is simplified as,

$$\rho \Theta \dot{\eta} - \rho \dot{\epsilon} + \sigma \dot{\epsilon} + \mu_0 H \dot{M} - \frac{1}{\Theta} \mathbf{q} \cdot \text{Grad } \Theta \geq 0. \quad (4)$$

Expression (4) represents the Clausius–Duhem inequality for a material that responds to thermal, mechanical and magnetic stimuli. The quantities involved in this inequality can be conceptually divided into the following subsets,

Independent variables:  $\{\epsilon, M, \eta\}$

Dependent variables:  $\{\sigma, H, \epsilon, \mathbf{q}, \Theta\}$  (5)

Balancing terms:  $\{r, \rho\}$ .

The independent variables or inputs can be arbitrarily specified as a function of space and time. The dependent variables or outputs are determined through response functions (constitutive equations) which depend on the history of the independent variables. Once the dependent variables are determined through response functions, the balancing terms are assigned the values that are necessary to satisfy the equations of motion. This conceptual division is chosen based on the form of the Clausius–Duhem inequality. However, the temperature  $\Theta$  is typically chosen as an independent variable instead of entropy as it is easier to measure and control. To accomplish the change of independent variable from  $\eta$  to  $\Theta$ , we replace the independent variable  $\epsilon$  with  $\psi$  through the Legendre transformation,

$$\psi = \epsilon - \Theta \eta, \quad (6)$$

where  $\psi$  is the specific Helmholtz energy potential. It is a free energy potential that represents the energy required to build a system at temperature  $\Theta$ . Combination of (4) and (6) gives,

$$-\rho \dot{\psi} - \rho \eta \dot{\Theta} + \sigma \dot{\epsilon} + \mu_0 H \dot{M} - \frac{1}{\Theta} \mathbf{q} \cdot \text{Grad } \Theta \geq 0. \quad (7)$$

We now assume isothermal conditions. This is because the coupled magnetomechanical behavior of interest in ferromagnetic shape memory Ni–Mn–Ga occurs in the low temperature martensite phase. The effect of changing temperature on the performance of Ni–Mn–Ga actuators and sensors is not considered in this study. The isothermal condition is represented as,

$$\dot{\Theta} = 0, \quad \text{Grad } \Theta = 0. \quad (8)$$



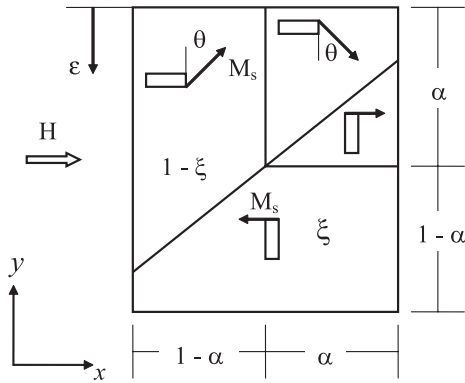


Figure 2. Simplified two-variant microstructure of Ni-Mn-Ga.

The Clausius–Duhem inequality (7) is reduced to a simplified form

$$-\rho\dot{\psi} + \sigma\dot{\varepsilon} + \mu_0 H \dot{M} \geq 0. \quad (9)$$

Implicit in (9) are the constitutive assumptions, or constitutive dependences,

$$\sigma = \sigma(\varepsilon, M) \quad H = H(\varepsilon, M) \quad \psi = \psi(\varepsilon, M). \quad (10)$$

For most of the applications involving magnetomechanical materials, such as sensing and actuation, the magnetic field is chosen as an independent variable as it is relatively easy to control by monitoring the current through a solenoid or an electromagnet. Magnetization, on the other hand, is usually more difficult to control, as this requires a feedback control system. To convert the set of independent variables  $(\varepsilon, M)$  to  $(\varepsilon, H)$ , a specific magnetic Gibbs energy  $\varphi$  is defined through the Legendre transformation,

$$\rho\varphi = \rho\psi - \mu_0 H M. \quad (11)$$

This leads to the inequality,

$$-\rho\dot{\varphi} + \sigma\dot{\varepsilon} - \mu_0 M \dot{H} \geq 0. \quad (12)$$

Inequality (12) is used to arrive at the constitutive response of the material for the sensing case. The Clausius–Duhem inequality for modeling of the actuation behavior is discussed in section 8.

### 3. Incorporation of the Ni-Mn-Ga microstructure in the thermodynamic framework

The framework discussed in section 2 pertains to thermo-magnetomechanical materials which have a perfect memory of their reference configuration and temperature. Similar to the thermal shape memory materials, FSMAs have imperfect memory, i.e., the materials when loaded and unloaded do not necessarily return to their initial undeformed configuration and temperature. One of the ways to model such a material is by introducing internal state variables in the argument list [53]. Internal state variables make it possible to extend the results

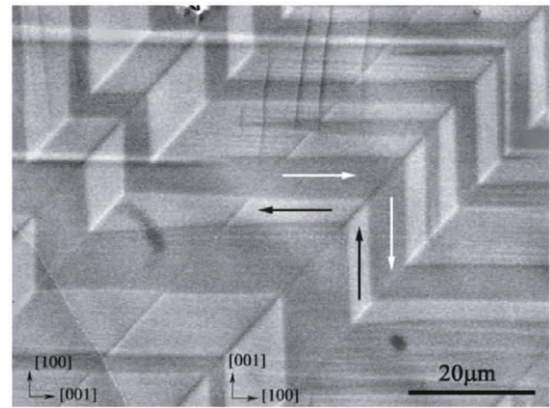


Figure 3. Image of twin-variant Ni-Mn-Ga microstructure by scanning electron microscope [54].

of thermoelastic theory to dissipative materials and account for certain microstructural phenomena.

Figure 2 shows the microstructure of single crystal Ni-Mn-Ga in the low temperature martensite phase. This microstructure is represented by three internal state variables: variant volume fraction  $\xi$ , domain fraction  $\alpha$ , and magnetization rotation angle  $\theta$ . These three variables account for the magnetic microstructure and the variant volume fraction accounts for the mechanical dissipation. This representation of the microstructure is motivated from experimental observations of single crystal Ni-Mn-Ga [54], which is shown in figure 3.

The applied field is oriented in the  $x$  direction, and the applied strain (or stress) is oriented in the  $y$  direction. The material is divided into regions which contain the crystals with their short, magnetically easy  $c$ -axes oriented perpendicular to one another. These regions are called variant volume fractions. The arrows indicate the magnetization vectors, and  $M_s$  denotes saturation magnetization. The two variants are separated by a twin boundary which is oriented at about  $45^\circ$  from the crystal axes. A field-preferred variant, with volume fraction  $\xi$ , is one in which the magnetically easy  $c$ -axis is aligned with the  $x$  direction. A stress-preferred variant, with volume fraction  $1 - \xi$ , is one in which the  $c$ -axis is aligned in the  $y$  direction. The evolution of the twin variants is termed *twin boundary motion* or *twin-variant rearrangement*, which results in the macroscopic deformation of the material due to the mismatch in the crystal dimensions. The twin boundary can be driven by either magnetic fields or mechanical stress.

It is assumed that the variant volume fractions are sufficiently large to be subdivided into  $180^\circ$  magnetic domains with volume fractions  $\alpha$  and  $1 - \alpha$ . This domain structure minimizes the net magnetostatic energy due to finite dimensions of the sample. In the absence of an external field, the domain fraction  $\alpha = 1/2$  leads to minimum magnetostatic energy. The high magnetocrystalline anisotropy energy of Ni-Mn-Ga dictates that the magnetization vectors in the field-preferred variant tend to remain attached to the crystallographic  $c$ -axis, i.e., they are oriented in the direction of the applied field or in the opposite direction. Any rotation of the magnetization vectors away from the  $c$ -axis results in an

increase in the anisotropy energy. The magnetization vectors in the stress-preferred variant are oriented at an angle  $\theta$  relative to the  $c$ -axis. Energy minimization dictates that the two magnetic domains within a stress-preferred variant are oriented at the same angle  $\theta$ , as shown in figure 2.

The concept of the thermomechanical process is now different than that described in the section 2. The independent variables are the strain  $\varepsilon$ , field  $H$  and the internal state variables  $\alpha$ ,  $\theta$ ,  $\xi$ . Therefore, the constitutive dependences for the sensing model are

$$\begin{aligned}\varphi &= \varphi(\varepsilon, H, \alpha, \theta, \xi) & \sigma &= \sigma(\varepsilon, H, \alpha, \theta, \xi) \\ M &= M(\varepsilon, H, \alpha, \theta, \xi).\end{aligned}\quad (13)$$

The rate of change of magnetic Gibbs energy can be expressed using the chain rule in the form

$$\rho\dot{\varphi} = \frac{\partial(\rho\varphi)}{\partial\varepsilon}\dot{\varepsilon} + \frac{\partial(\rho\varphi)}{\partial H}\dot{H} + \frac{\partial(\rho\varphi)}{\partial\alpha}\dot{\alpha} + \frac{\partial(\rho\varphi)}{\partial\theta}\dot{\theta} + \frac{\partial(\rho\varphi)}{\partial\xi}\dot{\xi}. \quad (14)$$

Combination of (12) and (14) gives

$$\begin{aligned}-\left[\frac{\partial(\rho\varphi)}{\partial\varepsilon}\dot{\varepsilon} + \frac{\partial(\rho\varphi)}{\partial H}\dot{H} + \frac{\partial(\rho\varphi)}{\partial\alpha}\dot{\alpha} + \frac{\partial(\rho\varphi)}{\partial\theta}\dot{\theta} + \frac{\partial(\rho\varphi)}{\partial\xi}\dot{\xi}\right] \\ + \sigma\dot{\varepsilon} - \mu_0 M\dot{H} \geq 0,\end{aligned}\quad (15)$$

which can be expanded as,

$$\begin{aligned}\left[\sigma - \frac{\partial(\rho\varphi)}{\partial\varepsilon}\right]\dot{\varepsilon} + \left[-\mu_0 M - \frac{\partial(\rho\varphi)}{\partial H}\right]\dot{H} \\ + \pi^\alpha\dot{\alpha} + \pi^\theta\dot{\theta} + \pi^\xi\dot{\xi} \geq 0.\end{aligned}\quad (16)$$

Here, the terms  $\pi^\alpha$ ,  $\pi^\theta$ , and  $\pi^\xi$  represent thermodynamic driving forces respectively associated with internal state variables  $\alpha$ ,  $\theta$ , and  $\xi$ . Note that these forces are defined as,

$$\begin{aligned}\pi^\alpha &:= -\frac{\partial(\rho\varphi)}{\partial\alpha}, & \pi^\theta &:= -\frac{\partial(\rho\varphi)}{\partial\theta}, \\ \pi^\xi &:= -\frac{\partial(\rho\varphi)}{\partial\xi}.\end{aligned}\quad (17)$$

In inequality (16), the terms  $\dot{\varepsilon}$  and  $\dot{H}$  are independent of each other, and of other rates. Therefore, for an arbitrary process, the coefficients of  $\dot{\varepsilon}$  and  $\dot{H}$  must vanish in order for the inequality to hold. This leads to the constitutive equations,

$$\sigma = \frac{\partial(\rho\varphi)}{\partial\varepsilon}, \quad (18)$$

$$M = -\frac{1}{\mu_0} \frac{\partial(\rho\varphi)}{\partial H}. \quad (19)$$

With these definitions, the Clausius–Duhem inequality reduces to

$$\pi^\alpha\dot{\alpha} + \pi^\theta\dot{\theta} + \pi^\xi\dot{\xi} \geq 0. \quad (20)$$

The constitutive equations or response functions for stress and magnetization are derived. These equations describe the material response under the given set of independent and dependent variables. Once the specific form of the magnetic Gibbs energy potential is constructed, expressions for the stress and magnetization can be obtained. The energy formulation is discussed in following section.

## 4. Energy formulation

The total thermodynamic free energy potential includes magnetic and mechanical components. The energy associated with the conventional magnetoelastic coupling is neglected, as the ordinary magnetostriction is around 100 times lower than the strain produced due to twin-variant rearrangement. Also, the energies associated with the thermal components are neglected as we are only concerned with isothermal behavior.

### 4.1. Magnetic energy

The total magnetic potential energy of the sample is a summation of the Zeeman energy, magnetostatic energy and magnetocrystalline anisotropy energy. Various magnetic energy components are given as a weighted summation of the energies of the two variants.

The Zeeman energy represents the work done by external magnetic fields on the material, or the energy available to drive twin boundary motion by magnetic fields. As seen in (11), the net magnetic Gibbs energy is a function of the internal or Helmholtz energy and the Zeeman energy. The Zeeman energy is minimum when the magnetization vectors are completely aligned in the direction of the externally applied field, and is maximum when the magnetization vectors are in opposite direction of the externally applied field. For the sensor/actuator model the Zeeman energy is

$$\begin{aligned}\rho\varphi_{ze} &= \xi[-\mu_0 H M_s \alpha + \mu_0 H M_s (1 - \alpha)] \\ &+ (1 - \xi)[- \mu_0 H M_s \sin \theta].\end{aligned}\quad (21)$$

The magnetostatic energy represents the self-energy due to the magnetization or the energy opposing the external work done by magnetic fields, on account of the geometry of the specimen. The magnetization creates a demagnetization field which tends to oppose the externally applied field. The strength of the demagnetization field depends on the geometry and permeability of the sample. A very long sample magnetized along its length has a very low demagnetization field as compared to the sample magnetized along its smallest dimension. The associated energy, or magnetostatic energy, tends to reduce the net magnetization of the material to zero by forming 180° domain walls. The magnetostatic energy is given by

$$\begin{aligned}\rho\varphi_{ms} &= \xi[\frac{1}{2}\mu_0 N (M_s \alpha - M_s (1 - \alpha))^2] \\ &+ (1 - \xi)[\frac{1}{2}\mu_0 N M_s^2 \sin^2 \theta],\end{aligned}\quad (22)$$

where  $N$  represents the difference in the demagnetization factors along the  $x$  and  $y$  directions [55] and it depends on the geometry of the specimen.

The magnetocrystalline anisotropy energy represents the energy needed to rotate a magnetization vector away from the magnetically easy  $c$ -axis. This energy is minimum (or zero) when the magnetization vectors are aligned along the  $c$ -axis and is maximum when they are rotated 90° away from the  $c$ -axis. In figure 2, all the contribution towards the anisotropy energy comes from the stress-preferred variant. The anisotropy energy is usually given in the form of a trigonometric power series for uniaxial symmetry. For Ni–Mn–Ga, it has been

observed that the approximation of up to the first term is usually sufficient to express the anisotropy energy, which is

$$\rho\varphi_{\text{an}} = (1 - \xi)[K_u \sin^2 \theta]. \quad (23)$$

The anisotropy constant,  $K_u$ , is calculated experimentally as the difference in the area under the easy- and hard-axis magnetization–field curves. It represents the energy associated with pure rotation of the magnetization vectors (hard axis) compared to the magnetization due to zero rotation of vectors (easy axis). Thus, the parameters required to calculate the magnetic energy component ( $M_s$  and  $K_u$ ) can be obtained from one experiment which measures the easy and hard-axis magnetization curves.

The contribution from magnetic energy in a given thermodynamic potential remains unchanged when modeling sensing, actuation and blocked force behavior. The magnetic component of the thermodynamic potential is

$$\rho\varphi_{\text{mag}} = \rho\varphi_{\text{ze}} + \rho\varphi_{\text{ms}} + \rho\varphi_{\text{an}}. \quad (24)$$

Thus,

$$\begin{aligned} \rho\varphi_{\text{mag}} = & \xi[-\mu_0 H M_s \alpha + \mu_0 H M_s (1 - \alpha) \\ & + \frac{1}{2} \mu_0 N (M_s \alpha - M_s (1 - \alpha))^2] + (1 - \xi) \\ & \times [-\mu_0 H M_s \sin \theta + \frac{1}{2} \mu_0 N M_s^2 \sin^2 \theta + K_u \sin^2 \theta]. \end{aligned} \quad (25)$$

#### 4.2. Mechanical energy

The mechanical energy represents the elastic strain energy contribution towards the internal or Helmholtz energy. For modelling the sensing effect, the expression for the mechanical energy depends on whether the process under consideration is strain loading ( $\dot{\xi} \leq 0$ ) or unloading ( $\dot{\xi} \geq 0$ ). Similar to the shape memory materials, the total strain is assumed to consist of an elastic component ( $\varepsilon_e$ ) and a twinning component ( $\varepsilon_{\text{tw}}$ ). Moreover, the twinning strain is proposed to be linearly proportional to the variant volume fraction,

$$\begin{aligned} \text{Loading: } \varepsilon_{\text{tw}} &= \varepsilon_0 (1 - \xi) & (\dot{\xi} \leq 0) \\ \text{Unloading: } \varepsilon_{\text{tw}} &= \varepsilon_0 \xi & (\dot{\xi} \geq 0) \end{aligned} \quad (26)$$

with  $\varepsilon_0$  being the maximum twinning strain,

$$\varepsilon_0 = 1 - c/a. \quad (27)$$

The mechanical loading arms are not glued to the sample, and the total strain depends on the distance of the loading arm with respect to its initial position. Therefore, the total strain during unloading accounts for the irreversible maximum twinning reorientation ( $\varepsilon_0$ ) that occurs after loading.

$$\begin{aligned} \text{Loading: } \varepsilon &= \varepsilon_e + \varepsilon_{\text{tw}} \\ \text{Unloading: } \varepsilon &= \varepsilon_e - \varepsilon_{\text{tw}} + \varepsilon_0. \end{aligned} \quad (28)$$

The discrepancy in the two equations arises because the undeformed or reference configuration is assumed to be in a completely unloaded state, which corresponds to  $\xi = 1$ . The

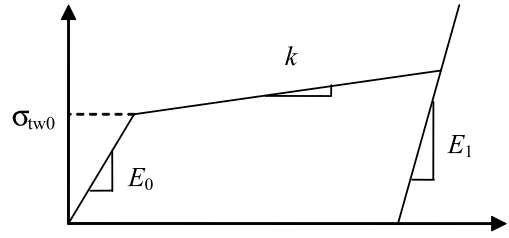


Figure 4. Schematic of stress–strain curve at zero bias field.

mechanical energy equation for both loading and unloading has the form

$$\rho\varphi_{\text{mech}} = \frac{1}{2} E(\xi) \varepsilon_e^2 + \frac{1}{2} a(\xi) \varepsilon_{\text{tw}}^2. \quad (29)$$

The first term in (29) represents the energy due to elastic strain, whereas the second term represents the energy due to twinning strain. The terms  $E(\xi)$ , and  $a(\xi)$  respectively represent effective moduli associated with elastic and twinning strains [6]. The parameters associated with the mechanical energy are obtained from the experimental stress–strain curve at zero bias field, shown schematically in figure 4. Modulus  $a(\xi)$  is obtained from the slope of twinning region  $k$  by analogy with two stiffnesses in series, having deformations equivalent to the elastic and twinning strains

$$\frac{1}{a(\xi)} = \frac{1}{E(\xi)} - \frac{1}{k}. \quad (30)$$

The compliance ( $S(\xi)$ ) of the material is considered to be a linear combination of the compliances at complete field-preferred state ( $S_0$ ) and complete stress-preferred state ( $S_1$ ). This linear average for effective material properties has been shown to be accurate for shape memory alloys and is equally appropriate for Ni–Mn–Ga [56, 57]. Therefore, the effective modulus is given as,

$$E(\xi) = \frac{1}{S(\xi)} = \frac{1}{S_0 + (1 - \xi)(S_1 - S_0)}. \quad (31)$$

The parameters ( $E_0 = 1/S_0$ ) and ( $E_1 = 1/S_1$ ) are obtained from the initial and final moduli as shown in figure 4.

The total magnetic Gibbs energy potential is the summation of magnetic and mechanical components,

$$\rho\varphi = \rho\varphi_{\text{mag}} + \rho\varphi_{\text{mech}}. \quad (32)$$

From equations (18), (26), (28), (29) and (32), the constitutive equation for stress for both loading and unloading cases is

$$\sigma = E(\xi) \varepsilon_e = E(\xi) [\varepsilon - \varepsilon_0 (1 - \xi)]. \quad (33)$$

The constitutive equation for magnetization is obtained from (19), (25) and (32) as,

$$M = M_s [2\xi\alpha - \xi + \sin \theta - \xi \sin \theta]. \quad (34)$$

The next step is to obtain the solutions for the evolution of the internal state variables ( $\alpha$ ,  $\theta$ ,  $\xi$ ) so that the macroscopic material response can be obtained from (33) and (34).

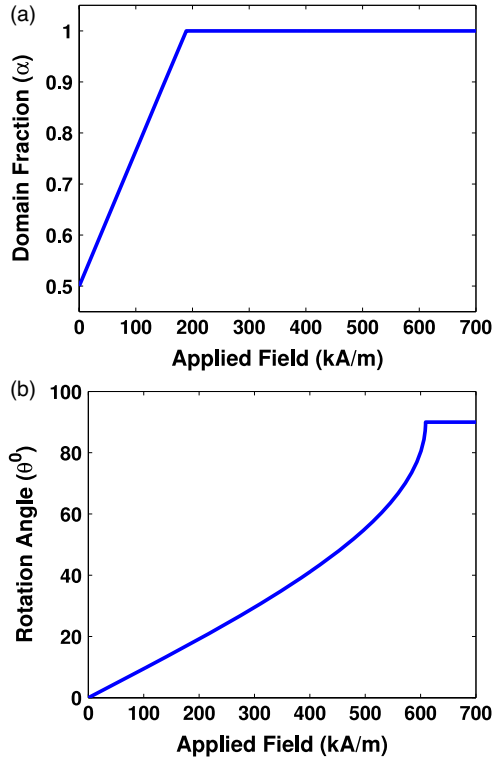


**Figure 5.** Variation of (a) domain fraction and (b) rotation angle with applied field.

### 5. Evolution of domain fraction and magnetization rotation angle

The evolution of domain fraction and rotation angle is associated with the magnetization change only, and is not directly related to the mechanical deformation of the material. The processes associated with the rotation of magnetization vectors and evolution of domain fraction are proposed to be reversible, because the easy-axis and hard-axis magnetization curves show negligible hysteresis. The easy-axis magnetization process involves evolution of domains, which is dictated by the magnitude of the magnetostatic energy opposing the Zeeman energy. The hard-axis magnetization process involves the rotation of magnetization vectors with respect to the easy  $c$ -axis of the crystals as dictated by the competition between the anisotropy energy and Zeeman energy. For reversible processes, the corresponding driving forces lead to zero increase in entropy. Hence, the driving forces themselves must be zero,

$$\pi^\alpha = -\frac{\partial(\rho\varphi)}{\partial\alpha} = 0, \quad (35)$$

$$\pi^\theta = -\frac{\partial(\rho\varphi)}{\partial\theta} = 0. \quad (36)$$

Closed form solutions for domain fraction and magnetization rotation angle are obtained from (25), (29), (32), (35), and (36),

$$\alpha = \frac{H}{2M_s N} + \frac{1}{2}, \quad (37)$$

$$\theta = \sin^{-1}\left(\frac{\mu_0 H M_s}{\mu_0 N M_s^2 + 2K_u}\right) \quad (38)$$

with the constraints  $0 \leq \alpha \leq 1$  and  $-\pi/2 \leq \theta \leq \pi/2$ . The variation of domain fraction and magnetization rotation angle is independent of variant volume fraction, and hence external strain or deformation. The dependence of these two internal variables on applied field is shown in figure 5.

### 6. Evolution of volume fraction

From (20), (35) and (36), the Clausius–Duhem inequality is reduced to

$$\pi^\xi \dot{\xi} \geq 0. \quad (39)$$

The total thermodynamic driving force associated with the evolution of volume fraction also includes magnetic and mechanical contributions.

$$\pi^\xi = \pi_{\text{mag}}^\xi + \pi_{\text{mech}}^\xi, \quad (40)$$

with the magnetic and mechanical driving forces given by

$$\begin{aligned} \pi_{\text{mag}}^\xi &= -\frac{\partial(\rho\varphi_{\text{mag}})}{\partial\xi} \\ &= \mu_0 H M_s \alpha - \mu_0 H M_s (1 - \alpha) \\ &\quad - \frac{1}{2} \mu_0 N (M_s \alpha - M_s (1 - \alpha))^2 \\ &\quad - \mu_0 H M_s \sin(\theta) + \frac{1}{2} \mu_0 N M_s^2 \sin^2(\theta) + K_u \sin^2(\theta), \end{aligned} \quad (41)$$

$$\begin{aligned} \text{Loading: } \pi_{\text{mech}}^\xi &= -\frac{\partial(\rho\varphi_{\text{mech}})}{\partial\xi} = -E(\xi)[\varepsilon - \varepsilon_0(1 - \xi)]\varepsilon_0 \\ &\quad - \frac{1}{2} \frac{\partial E(\xi)}{\partial\xi} [\varepsilon - \varepsilon_0(1 - \xi)]^2 \\ &\quad + a(\xi)(1 - \xi)\varepsilon_0^2 - \frac{1}{2} \frac{\partial a(\xi)}{\partial\xi} \varepsilon_0^2 (1 - \xi)^2, \end{aligned} \quad (42)$$

$$\begin{aligned} \text{unloading: } \pi_{\text{mech}}^\xi &= -\frac{\partial(\rho\varphi_{\text{mech}})}{\partial\xi} \\ &= -E(\xi)[\varepsilon - \varepsilon_0(1 - \xi)]\varepsilon_0 - \frac{1}{2} \frac{\partial E(\xi)}{\partial\xi} [\varepsilon - \varepsilon_0(1 - \xi)]^2 \\ &\quad - a(\xi)\varepsilon_0^2 \xi - \frac{1}{2} \frac{\partial a(\xi)}{\partial\xi} \varepsilon_0^2 \xi^2. \end{aligned} \quad (43)$$

The start of the twinning process in shape memory materials and FSMA requires the overcoming of a finite energy threshold associated with the twinning stress. This is evident from the stress–strain plots at zero field shown in figure 4, and also from strain field plots [42, 10], where a finite threshold field needs to be overcome. The associated energy or critical driving force ( $\pi^{\text{cr}}$ ) required for twin-variant rearrangement to start is estimated from the twinning stress at zero field ( $\sigma_{\text{tw}0}$ )

$$\pi^{\text{cr}} = \sigma_{\text{tw}0} \varepsilon_0. \quad (44)$$

This twinning barrier conceptually represents the work required to rotate a single crystal, which is therefore the product of the associated force ( $\sigma_{\text{tw}0}$ ) and deformation ( $\varepsilon_0$ ). During loading, the stress-preferred variants grow at the expense of field-preferred variants, implying  $\dot{\xi} \leq 0$ . Thus the driving force  $\pi^\xi$  must be negative for inequality (39) to be satisfied. The growth of stress-preferred variants begins when



the total driving force reaches the negative value of the critical driving force. The value of  $\xi$  is then obtained by numerically solving the relation,

$$\pi^\xi = -\pi^{\text{cr}}. \quad (45)$$

During unloading, the field-preferred variants grow, hence  $\dot{\xi} \geq 0$ . Thus, the driving force  $\pi^\xi$  has to be positive in order for inequality (39) to be satisfied. When the total force reaches the positive critical driving force, the evolution of  $\xi$  is initiated. The subsequent values of  $\xi$  are obtained by numerically solving the equation

$$\pi^\xi = \pi^{\text{cr}}. \quad (46)$$

Once  $\alpha$ ,  $\theta$ , and  $\xi$  are determined, the stress  $\sigma$  and magnetization  $M$  are found from (33) and (34), respectively. It is noted that  $\xi$  is restricted so that  $0 \leq \xi \leq 1$ .

## 7. Sensing model results

The equations in sections 2–6 are solved using MATLAB. The equations are solved in an iterative manner to check the twin onset condition at each step. Also, the restrictions are imposed so certain variables do not exceed their physical limits.

### 7.1. Stress–strain results

Calculated stress–strain plots at bias fields ranging from 94 to 368 kA m<sup>−1</sup> are compared with experimental measurements in figure 6. The parameters used for model calculations are:  $E_0 = 400$  MPa,  $E_1 = 2400$  MPa,  $\sigma_{\text{tw}0} = 0.6$  MPa,  $k = 14$  MPa,  $\varepsilon_0 = 0.058$ ,  $K_u = 1.67 \times 10^5$  J m<sup>−3</sup>,  $M_s = 625$  kA m<sup>−1</sup>,  $N = 0.308$ . The initial high-slope region is produced by the elastic compression of the material, which takes place until a certain critical stress is reached. Once the critical stress is reached, the twin-variant rearrangement starts, represented by the low-slope region. This low-slope region continues until the twin-variant rearrangement is complete. Beyond this state, the material again is compressed elastically. During unloading, the material follows similar behavior, i.e., elastic expansion followed by twin-variant rearrangement in the reverse direction. However, the behavior during unloading depends on the magnitude of the bias field. At low bias fields, the material does not return to its original shape, whereas at medium and high bias fields the material respectively shows a partial and complete recovery of its original shape. Thus, increasing bias fields reveal the transition from irreversible to reversible behavior. For the applied bias field used in this study, the model accurately describes the shape of the hysteresis loop and the amount of pseudoelasticity or residual strain at which the sample returns to zero stress.

As the bias field is increased, more energy is required for twin-variant rearrangement to start, resulting in an increase in the twinning stress. The twinning stress at a given bias field corresponds to the situation where the net thermodynamic driving force is equal to the critical driving force ( $\pi^\xi = -\pi^{\text{cr}}$ ) and also the material is in complete field-preferred state

( $\xi = 1$ ). Therefore, an expression for the twinning stress can be obtained as detailed below:

$$\pi_{\text{mag}}^\xi + \pi_{\text{mech}}^\xi = -\pi^{\text{cr}}$$

At start of twinning ( $\xi = 1$ ),

$$\pi_{\text{mag}}^\xi(H) - \sigma_{\text{tw}}(H)\varepsilon_0 = -\sigma_{\text{tw}0}\varepsilon_0 \quad (47)$$

$$\sigma_{\text{tw}}(H) = \frac{\pi_{\text{mag}}^\xi(H)}{\varepsilon_0} + \sigma_{\text{tw}0}.$$

Figure 7 shows the dependence of the twinning stress on the applied bias field, calculated from the experiments and the model. The model accurately quantifies the monotonic increase in twinning stress with increasing bias field. This result is an improvement over an earlier model [7], in which the twinning stress was constant below fields of 195 kA m<sup>−1</sup>. The twinning stress–field curve shows a sigmoid shape, which eventually saturates at high magnetic fields. This indicates that the stress–strain behavior will remain unchanged when the applied bias field is greater than the saturation field.

### 7.2. Flux density results

In order to compare the model results with flux density measurements [6], the magnetic induction or flux density ( $B_m$ ) is calculated from magnetization (34) by means of the relation

$$B_m = \mu_0(H + N_x M), \quad (48)$$

where  $N_x$  is the demagnetization factor in the  $x$  direction [58]. It is seen that for the same magnetization, the measured flux density depends on the geometry of the sample.

The flux density plots shown in figure 8 are of interest for sensing applications. The absolute value of flux density decreases with increasing compressive stress. As the sample is compressed from its initial field-preferred variant state ( $\xi = 1$ ), the stress-preferred variants grow at the expense of field-preferred variants. Due to the high magnetocrystalline anisotropy of Ni–Mn–Ga, the nucleation and growth of stress-preferred variants occurs in concert with the rotation of magnetization vectors into the longitudinal direction, which causes a reduction of the permeability and flux density in the transverse direction. The curves obtained from model calculations show less hysteresis than the measurements and a slight nonlinearity in the relationship between flux density and strain. This is in agreement with measurements by Straka *et al* [23] in which the magnetization dependence on strain is almost linear and exhibits very little hysteresis. As shown in figure 8(b), the model accurately quantifies the dependence of flux density on stress. While the tests were conducted in displacement control, the observed trends should resemble those obtained experimentally with stress as the independent variable.

The overall change in flux density from the initial state ( $\xi = 1$ ) to the final state ( $\xi = 0$ ) is a function of applied bias field. Because of the almost linear nature of the flux–strain ( $B$ – $\varepsilon$ ) curve, the slope of this curve at a given strain is defined as sensitivity, or a factor similar to piezoelectric coupling

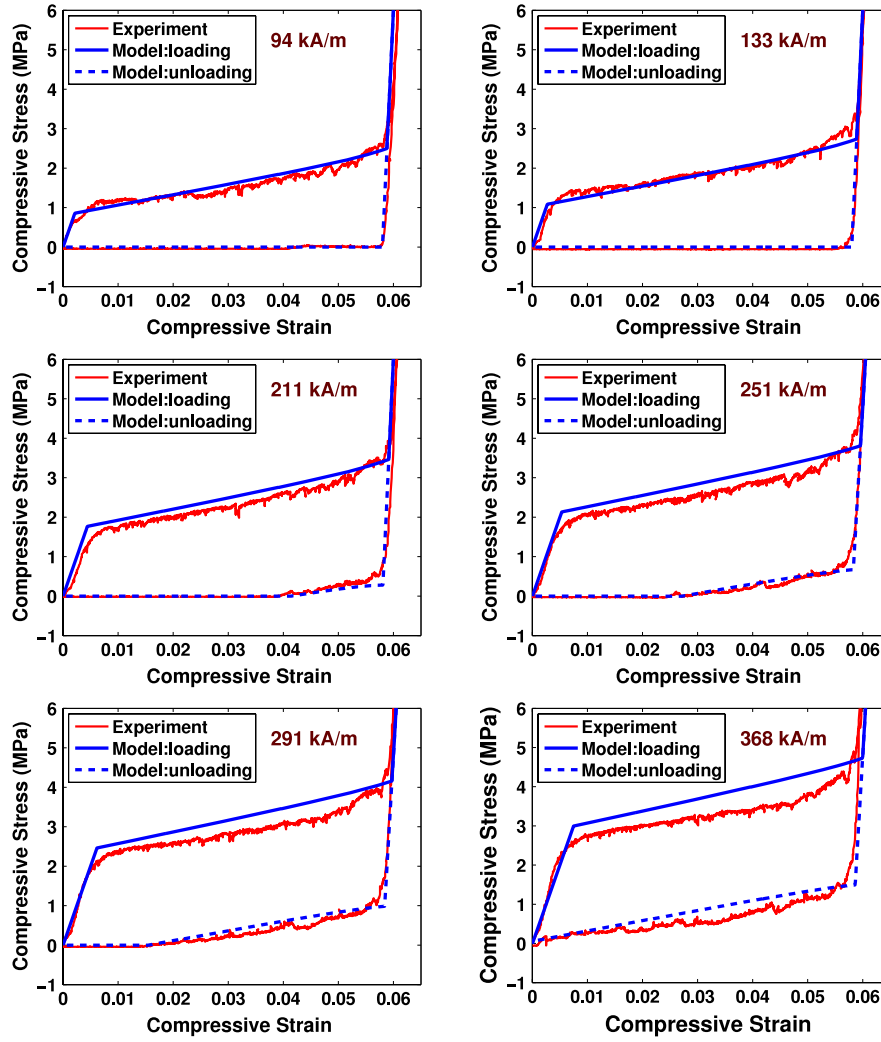


**Figure 6.** Stress–strain plots at varied bias fields. Dotted line: experiment; solid line: calculated (loading); dashed line: calculated (unloading).

coefficient at constant field,  $(\partial B / \partial \varepsilon)^H$ . This sensitivity factor is defined as the slope at mid-range (3% strain) in the loading path of the flux–strain curve. The variation of this factor with bias field is shown in figure 9. The experimental values of sensitivity factor are approximated to the ratio of total flux density change to the associated strain range.

This behavior can be explained from the easy- and hard-axis flux density curves of Ni–Mn–Ga. The easy-axis curve corresponds to the state in which the sample is in complete field-preferred state, whereas the hard-axis curve corresponds to the state of the sample when the sample is in complete stress-preferred state. Therefore, the expressions for the easy-axis ( $\xi = 1$ ) and hard-axis ( $\xi = 0$ ) magnetization as a function of magnetic field can be obtained from (34), (37) and (38), giving

$$M_{\text{easy}} = M_{(\xi=1)} = \frac{H}{N}$$

$$M_{\text{hard}} = M_{(\xi=0)} = \frac{\mu_0 H M_s^2}{\mu_0 N M_s^2 + 2K_u} \quad (49)$$

If  $M > M_s$ ,  $M = M_s$ .

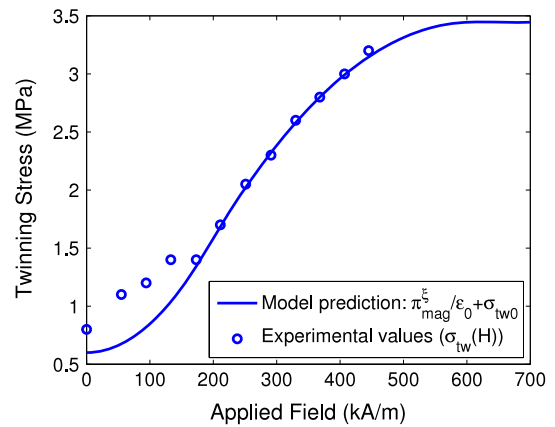


**Figure 7.** Variation of twinning stress with applied bias field.

Model results for easy-axis and hard-axis magnetization and flux density are shown in figures 10(a) and (b), respectively. When the sample is compressed at a given constant field, the flux density changes from the corresponding easy-axis

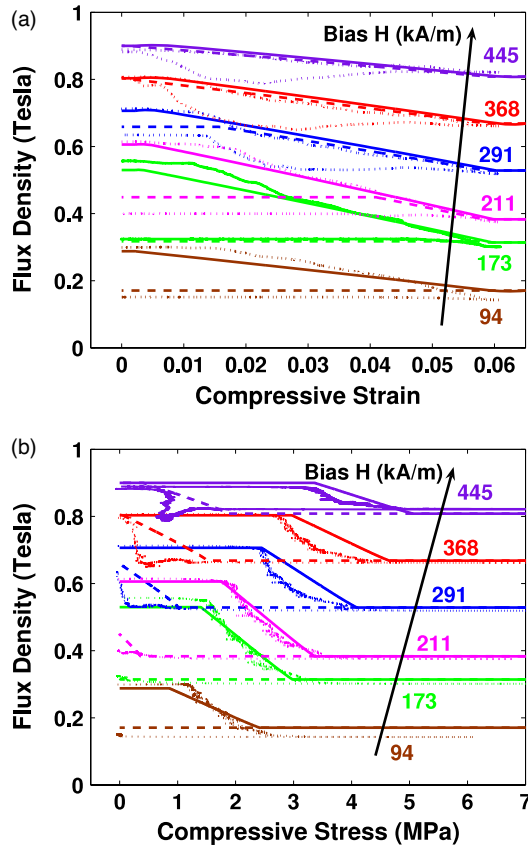


**Figure 8.** Model results for (a) flux density–strain and (b) flux density–stress curves. Dotted line: experiment; solid line: calculated (loading); dashed line: calculated (unloading).

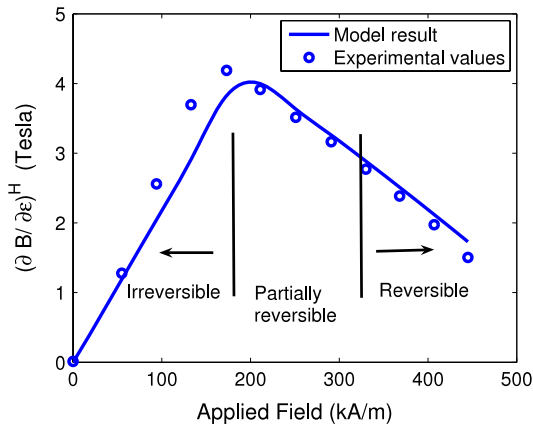


**Figure 9.** Variation of sensitivity factor with applied bias field.

value to the corresponding hard-axis value. Hence, the optimum sensing range occurs when the two curves are at the maximum distance from each other and the sample shows pseudoelastic behavior. At a bias field of  $368 \text{ kA m}^{-1}$ , a reversible flux density change of  $145 \text{ mT}$  is obtained over a range of  $5.8\%$  strain and  $4.4 \text{ MPa}$  stress. This makes the magnetic field of  $368 \text{ kA m}^{-1}$  the optimum bias field to obtain maximum reversible sensing from the material.

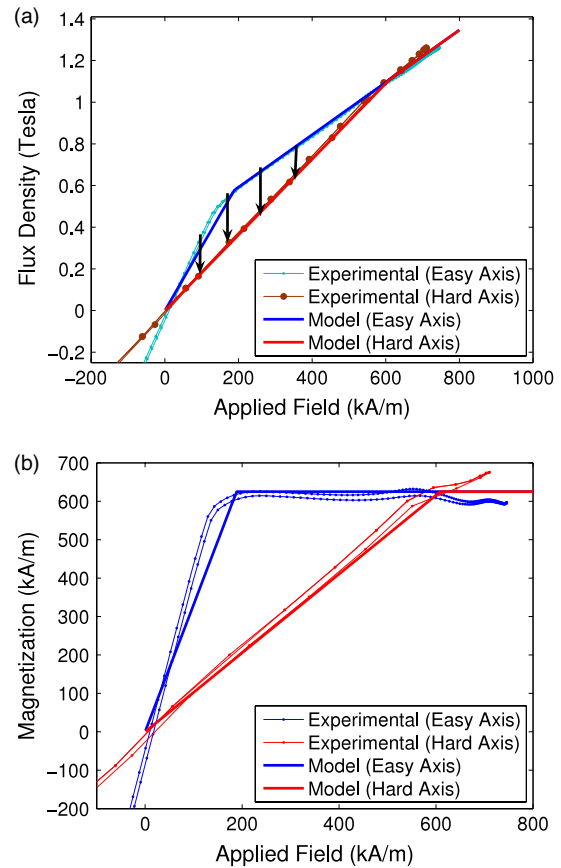


**Figure 10.** Model results for easy-axis and hard-axis curves. (a) flux density versus field; (b) magnetization versus field.

The Ni–Mn–Ga alloy investigated here therefore shows potential for high-compliance, high-displacement deformation sensors.

### 7.3. Thermodynamic driving force and volume fraction

The volume fraction dictates the deformation of the material and is the only variable that is responsible for the coupling between the magnetic and mechanical domains. Therefore, the evolution of volume fraction and the corresponding thermodynamic driving forces provide key insight into the material's behavior. The driving forces are calculated from equations (41), (42) and (43), and the volume fraction is obtained by numerically solving equations (45) and (46).

The evolution of the thermodynamic driving forces acting on a twin boundary with increasing compressive strain is shown in figure 11 for several bias fields. It is seen that the driving force due to stress is negative since the stress is compressive, and more importantly, it opposes the growth of volume fraction  $\xi$ . Conversely, the driving force due to magnetic field is positive indicating that the field favors the growth of volume fraction  $\xi$ . During loading, the total force has to overcome the negative critical driving force ( $-\pi^{\text{cr}}$ ) for twin-variant rearrangement to start. Similarly, during unloading, the total force has to overcome the positive critical driving force ( $\pi^{\text{cr}}$ ) for the start of twin-variant rearrangement

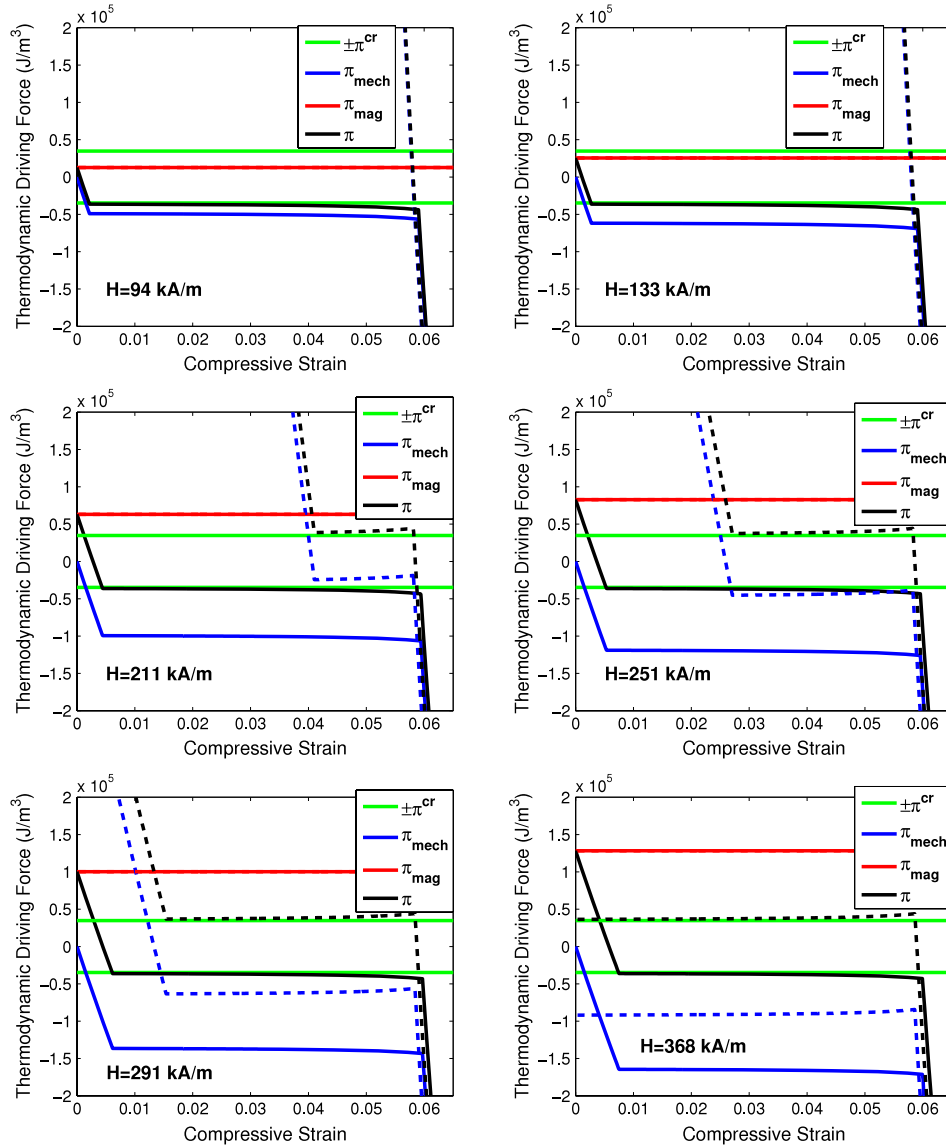


Figure 11. Evolution of thermodynamic driving forces.

in the opposite direction. The magnitudes of total driving force during twin-variant rearrangement for loading and unloading are negative and positive, respectively, in order for Clausius–Duhem inequality (39) to be satisfied. Once the twin boundary motion is initiated, the total driving force remains at almost the same value as the critical driving force value. These principles hold true for the actuation model also. The corresponding variation in the variant volume fraction is shown in figure 12.

There is a strong correlation between stress–strain (figure 6) and flux density–strain (figure 8(a)) regarding the reversibility of the magnetic and mechanical behavior. Because a change in flux density relative to the initial field-preferred single variant is directly associated with the growth of stress-preferred variants, the flux density value returns to its initial value only if the stress–strain curve exhibits magnetic field induced pseudoelasticity. The model calculations accurately reflect this trend, as seen by the variation of residual strain with bias field shown in figure 13.

## 8. Extension to actuation model

The framework developed for the sensing model is extended to model the actuation behavior of Ni–Mn–Ga, i.e., dependence of strain and magnetization on varying field under bias compressive stress. The actuator model utilizes the exact same parameters as the sensing model. Further, the actuation model framework is consistent with previous models by Kiefer and Lagoudas [42] and Faidley *et al* [45]. In a typical Ni–Mn–Ga actuator, the material is subjected to a bias stress or prestress using a spring. The initial configuration of the material is usually its shortest length ( $\xi = 0$ ). In the presence of bias stress, an external field is applied to generate strain against the mechanical load. During increasing field ( $|\dot{H}| > 0$ ), the material does the work by expanding against the prestress and strain is generated. During reverse field application ( $|\dot{H}| < 0$ ), if the prestress is sufficiently large, the original length of the sample is restored to complete one strain cycle.



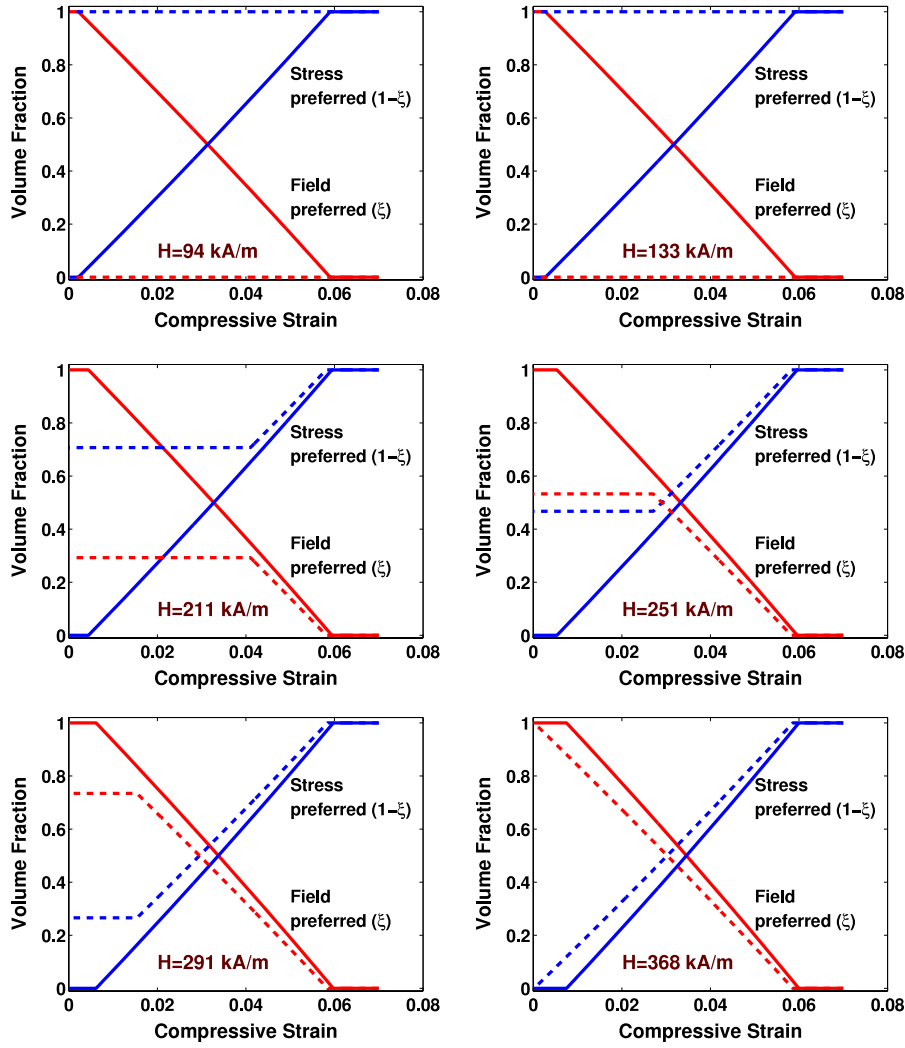


Figure 12. Evolution of volume fraction.

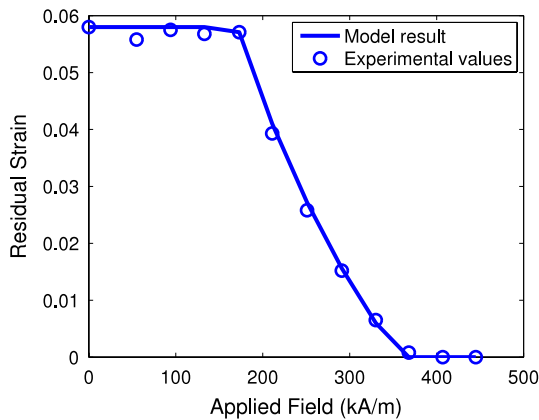


Figure 13. Variation of residual strain with applied bias field.

### 8.1. Actuation model

In the actuator model, the applied field and bias stress constitute independent variables, whereas the generated strain and magnetization constitute the dependent variables. To arrive

at the desired set of independent variables  $(H, \sigma)$  from the original  $(M, \varepsilon)$  variables seen in (9), the model is formulated by defining the specific Gibbs energy  $(\phi)$  as thermodynamic potential via a Legendre transform,

$$\rho\phi = \rho\psi - \sigma\varepsilon_e - \mu_0 HM. \quad (50)$$

Gibbs free energy is a thermodynamic potential which conceptually represents the amount of useful work obtainable from a system. It is obtained by subtracting the work done by external magnetic field and mechanical stress from the Helmholtz energy. From (9) and (50), a Clausius–Duhem inequality is obtained, which has the form,

$$-\rho\dot{\phi} - \dot{\sigma}\varepsilon_e - \mu_0 M\dot{H} + \sigma\dot{\varepsilon}_{tw} \geq 0, \quad (51)$$

where the twinning strain component is

$$\varepsilon_{tw} = \varepsilon_0 \xi. \quad (52)$$

The actuator under consideration has the constitutive dependences,

$$\begin{aligned} \phi &= \phi(\sigma, H, \xi, \alpha, \theta) & \varepsilon &= \varepsilon(\sigma, H, \xi, \alpha, \theta) \\ M &= M(\sigma, H, \xi, \alpha, \theta). \end{aligned} \quad (53)$$

The domain fraction, rotation angle and variant volume fraction constitute the internal state variables as in the sensing model. Following the Coleman–Noll procedure similar to that employed to develop the sensing model in section 3, we arrive at the constitutive equations

$$\varepsilon_e = -\frac{\partial(\rho\phi)}{\partial\sigma}, \quad (54)$$

$$M = -\frac{1}{\mu_0} \frac{\partial(\rho\phi)}{\partial H}. \quad (55)$$

The Clausius–Duhem inequality reduces to the form,

$$\left(-\frac{\partial(\rho\phi)}{\partial\xi} + \sigma\varepsilon_0\right)\dot{\xi} \geq 0, \quad (56)$$

$$\pi^{\xi*} \dot{\xi} \geq 0, \quad (57)$$

where the total thermodynamic driving force  $\pi^{\xi*}$  is defined as

$$\begin{aligned} \pi^{\xi*} &= -\frac{\partial(\rho\phi)}{\partial\xi} + \sigma\varepsilon_0 = \pi^\xi + \sigma\varepsilon_0 \\ &= \pi_{\text{mag}}^\xi + \pi_{\text{mech}}^\xi + \sigma\varepsilon_0. \end{aligned} \quad (58)$$

The contribution of the magnetic energy to the total Gibbs energy remains the same as (25). Therefore, the evolution equations for domain fraction (37), rotation angle (38) and magnetic driving force (41) remain intact. The mechanical energy contribution to the Gibbs energy is

$$\rho\phi_{\text{mech}} = -\frac{1}{2}S\sigma^2 + \frac{1}{2}a\varepsilon_0^2\xi^2. \quad (59)$$

Here, the first term represents the elastic Gibbs energy due to bias stress, while the second term represents the energy due to twinning. Unlike in the sensing model, the mechanical energy equation for actuation remains the same during application of both increasing and decreasing fields. The parameters associated with the mechanical energy are the same as those presented for the sensing model, except compliance. An average value of compliance ( $S$ ) is used, which is the inverse of the average elastic modulus ( $E$ ).

The undeformed configuration for the actuation process represents the sample at its minimum length ( $\xi = 0$ ) in the presence of a compressive bias stress  $\sigma$ . This bias stress compresses the sample elastically, as the sample is already in the complete stress-preferred variant state. When the magnetic field is increased, the driving force due to the field starts acting opposite to the driving force due to stress. The expression for net mechanical thermodynamic driving force is

$$\pi_{\text{mech}}^{\xi*} = -a\varepsilon_0^2\xi + \sigma\varepsilon_0. \quad (60)$$

When the applied field increases ( $|\dot{H}| \geq 0$ ), the volume fraction tends to increase ( $\dot{\xi} \geq 0$ ). When the total thermodynamic driving force exceeds the positive critical value  $\pi^{\text{cr}}$ , twin boundary motion is initiated. The numerical value of volume fraction  $\xi$  can be obtained by solving the relation

$$\pi^{\xi*} = \pi^{\text{cr}}. \quad (61)$$

When the field decreases ( $|\dot{H}| \leq 0$ ), the stress-preferred variants start to grow ( $\dot{\xi} \leq 0$ ) if the field becomes sufficiently

low, provided the bias compressive stress is strong enough to start twin boundary motion in the opposite direction. If the total driving force becomes lower than the negative of the critical driving force, the volume fraction is obtained by solving

$$\pi^{\xi*} = -\pi^{\text{cr}}. \quad (62)$$

Finally, from the values of  $\alpha$ ,  $\theta$ , and  $\xi$ , magnetization is obtained from (34) and total strain is obtained by addition of elastic and twinning components,

$$\varepsilon = \varepsilon_e + \varepsilon_{\text{tw}}. \quad (63)$$

## 8.2. Actuation model results

The model validation and identification of model parameters is conducted by comparison of model results with experimental data published by Murray *et al* [51]. A  $14 \times 14 \times 6$  mm<sup>3</sup> single crystal Ni–Mn–Ga sample was subjected to slowly alternating magnetic fields of amplitude 750 kA m<sup>−1</sup> in the presence of compressive bias stresses ranging from 0 to 2.11 MPa. The magnetic field was applied using an electromagnet, whereas the bias stresses were applied using dead weights. The initial configuration of the sample was a complete stress-preferred state, which enabled generation of full 6% strain under saturating fields. The model parameters utilized in the actuation model are:  $E = 800$  MPa,  $\sigma_{\text{tw}0} = 0.8$  MPa,  $k = 14$  MPa,  $\varepsilon_0 = 0.058$ ,  $K_u = 1.7 \times 10^5$  J m<sup>−3</sup>,  $M_s = 520$  kA m<sup>−1</sup>,  $N = 0.239$ .

**8.2.1. Strain–field.** The model results for strain dependence on field at varied bias stresses are shown in figure 14. With increasing field, the material does not start deforming until the coercive field is reached. Further deformation occurs with a rapid increase in strain for a relatively small magnetic field range. This region corresponds to the twin boundary motion where the thermodynamic driving force due to magnetic field exceeds that due to the bias stress. Depending on the magnitude of the bias field, a saturating strain is reached, after which the material does not deform with further application of magnetic field. This saturation strain or the maximum magnetic field induced strain is a function of the bias stress. When the field is removed, the material does not return to its original shape unless the applied bias stress is sufficiently large. The increasing bias stress marks the transition from irreversible to reversible behavior. This effect is analogous to that of the bias field in the sensing study. With increasing bias stress, the total strain produced decreases monotonically, and the coercive field required to initiate twin boundary motion increases. For most of the bias stress values, the model results both for the forward and return path accurately match the measurements.

**8.2.2. Maximum strain.** The maximum magnetic field induced strain is of interest for actuation applications. For the saturating field, the maximum strain is obtained from

$$\begin{aligned} \pi_{\text{mag}}^\xi(H_{\text{sat}}) + \pi_{\text{mech}}^\xi &= \pi^{\text{cr}} & \xi_{\text{max}} &= \frac{K_u + \sigma_b\varepsilon_0 - \pi^{\text{cr}}}{a\varepsilon_0^2} \\ \varepsilon(H_{\text{sat}}) &= S\sigma_b + \varepsilon_0\xi_{\text{max}}. \end{aligned} \quad (64)$$

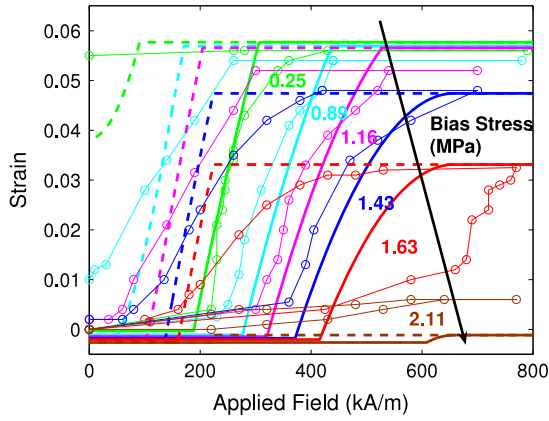


**Figure 14.** Strain–applied field at varied bias stresses. Dotted line: experiment; solid line: calculated (loading); dashed line: calculated (unloading).

The maximum thermodynamic driving force at the saturating field is equal to the anisotropy constant ( $K_u$ ). The model accurately quantifies the maximum magnetic field induced deformation at different bias stresses ranging from 0.25 to 2.11 MPa. According to the model, the bias stresses of 0.89 and 1.16 MPa can be considered as optimum where a completely reversible strain of maximum magnitude is obtained. A comparison between calculations and experimental data is shown in figure 15.

**8.2.3. Coercive field.** Coercive field is the field at which twin-variant rearrangement starts during forward field application ( $|\dot{H}| \geq 0$ ). Evaluation of the coercive field is important as it dictates the strength of magnetic field required to actuate the material. As seen in figure 14, once the coercive field is exceeded, the subsequent twin-variant rearrangement occurs with relatively smaller increase in the magnetic field. Therefore, accurate evaluation of the coercive field gives an estimate of the magnetic field requirements for the electromagnet design. The coercive field determines the resistance to the twin boundary motion due to the added contributions of internal material dislocations (twinning stress) and the compressive bias stress. It is an analogous quantity to the twinning stress in the sensing behavior: the coercive field increases with increasing bias stress in actuation, whereas the twinning stress increases with increasing bias field in sensing.

When the applied field equals the coercive field, the net thermodynamic driving force equals the critical value ( $\pi^{\xi^*} = \pi^{\text{ct}}$ ), and the material consists of a single stress-preferred variant ( $\xi = 0$ ). Under these conditions, the expression for the domain fraction is reduced to  $\alpha = 1$ , as the magnetic field is assumed to be strong enough to transform the material into a single domain. The expression for the magnetization rotation angle  $\theta$  remains intact as given by (38). Using these properties, the coercive field ( $H_c$ ) is obtained by solving

$$\begin{aligned}
 & -\mu_0 H_c M_s \sin \theta + 2\mu_0 H_c M_s \alpha - \mu_0 H_c M_s \\
 & - 2\mu_0 N M_s^2 \alpha^2 + 2\mu_0 N M_s^2 \alpha + \sigma_b \varepsilon_0 \\
 & + K_u - \frac{1}{2} \mu_0 N M_s^2 \cos^2 \theta - K_u \cos^2 \theta = \sigma_{\text{tw}0} \varepsilon_0. \quad (65)
 \end{aligned}$$

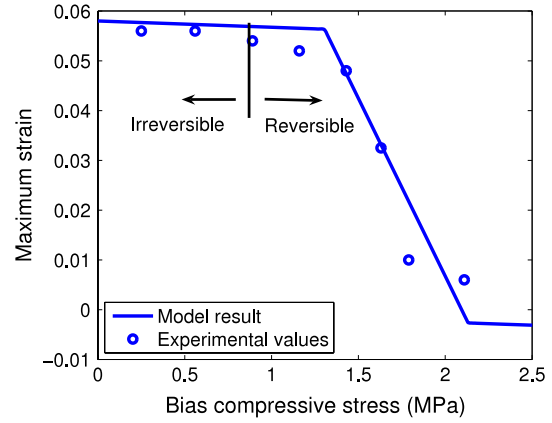


**Figure 15.** Variation of maximum magnetic field induced strain with bias stress.

The expression for the coercive field is therefore

$$\begin{aligned}
 H_c = & \left\{ \mu_0 N M_s^2 + 2K_u \right. \\
 & \left. - \sqrt{2\mu_0 N M_s^2 [K_u + \varepsilon_0 (\sigma_b - \sigma_{\text{tw}0})] + 4K_u \varepsilon_0 (\sigma_b - \sigma_{\text{tw}0}) + 4K_u^2} \right\} \\
 & \times \{\mu_0 M_s\}^{-1} \quad (66)
 \end{aligned}$$

which is obtained from (41), (44), and (61). Although the twinning stress at zero field ( $\sigma_{\text{tw}0}$ ) and the bias stress ( $\sigma_b$ ) have opposite signs in equation (66), it must be noted that the twinning stress at zero field is defined as positive for compression whereas the bias stress is defined as negative for compression. Thus, the bias stress *adds* to the resistance applied by the twinning stress to the twin-variant rearrangement. Therefore, the coercive field increases with increase in bias stress. Figure 16 shows the variation of the coercive field with the bias stress. The model results are in overall agreement with the experimental data. The dependence of the coercive field on the bias stress resembles a parabolic pattern, and it increases rapidly as bias stress increases. Therefore, the optimum bias stress is desired to be as low as possible in order to keep the coercive field at a reasonably low value. A lower coercive field facilitates a compact electromagnet.

**8.2.4. Magnetization–field.** Model calculations for the magnetization dependence on field are shown in figure 17. The hysteretic magnetization curves illustrate that the volume fraction varies during increasing and decreasing field application. The initial part of the magnetization curve at all bias stresses resembles the hard-axis curve, as the material initially consists of only one variant preferred by stress. When the twin boundary motion starts, the curve rapidly goes to saturation indicating transition into a field-preferred variant state. When the field is decreasing, the curve resembles the easy-axis magnetization curve in the case in which there is zero or very little evolution of stress-preferred variants (0.25 MPa). With increasing bias stresses, the magnetization curve tends to shift away from the easy-axis curve during field reversal. At bias stress of 2.11 MPa, where twin boundary motion is

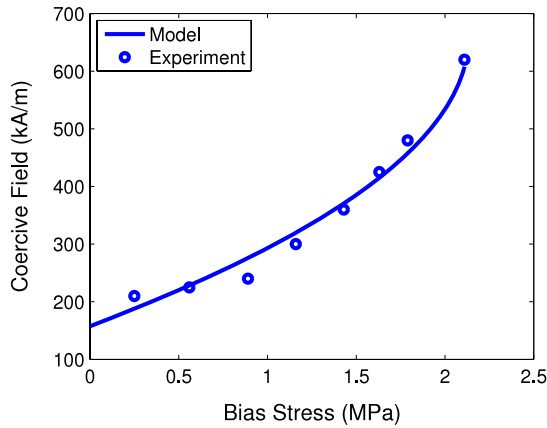


**Figure 16.** Variation of the coercive field with bias stress.

almost suppressed, the behavior is similar to the hard-axis curve during both forward and reverse field application.

### 9. Blocked force model

The force generated by a Ni–Mn–Ga sample in partially blocked conditions during actuation measurements was presented by Henry [59] and O’Handley *et al* [28]. Their measurements suggest the presence of significant magnetoelastic coupling: as the transverse magnetic field was increased below the field required to initiate twin boundary motion, the measured stress increased even though the sample and spring remained undeformed. Because a spring was used to precompress the sample in the axial direction, some amount of detwinning was allowed and hence the blocking stresses were not measured. Further, no model for magnetization was presented. Force measurements under completely mechanically blocked conditions at different bias strains were presented by Jaaskelainen *et al* [60] and recently by Couch and Chopra [61]. Neither magnetization measurements nor analytical models were included. Likhachev *et al* [21] presented an expression for the thermodynamic driving force induced by magnetic fields acting on the twin boundary. This force depends on the derivative of the magnetic energy difference between the hard-axis and easy-axis configurations. Although this force is useful in modeling the strain–field and stress–strain behavior, its origin is not well understood. Further, this force is independent of the volume fraction, thus it cannot accurately model the stress–field behavior, in which the net generated stress varies with bias strain (see figure 21). The behavior of Ni–Mn–Ga under constant stress of 0.6 and 3 MPa was characterized and modeled by Ma and Li [62], who demonstrated the effect of unconstrained and constrained twin-variant reorientation on the magnetization of Ni–Mn–Ga. Landis [63] presented a continuum thermodynamics formulation to investigate the interactions between magnetic domain walls and martensite twin-variant reorientation, and developed an expression for the critical blocking stress.

The available blocking stress, defined as the maximum field induced stress relative to the bias stress, is critical for quantifying the work capacity of an active material. In this

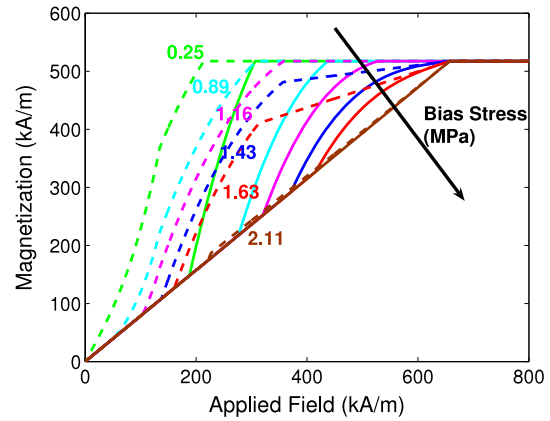


**Figure 17.** Magnetization–applied field at several bias stresses. Dotted line: experiment; solid line: calculated (loading); dashed line: calculated (unloading).

study we characterize and model the magnetic field induced stress and magnetization generated by a commercial Ni–Mn–Ga sample (AdaptaMat Ltd) when it is prevented from deforming. We refer to this type of mechanical boundary as ‘mechanically blocked condition’. The material is first compressed from its longest shape to a given bias strain (which requires a corresponding bias stress) and is subsequently subjected to a slowly alternating magnetic field while being prevented from deforming. The tests are repeated for several bias strains.

The experimental setup is the same as for sensing characterization, which consists of a custom-made electromagnet and a uniaxial stress stage. A  $6 \times 6 \times 10 \text{ mm}^3$  Ni–Mn–Ga sample (AdaptaMat Ltd) is placed in the center gap of the electromagnet. The sample exhibits a free magnetic field induced deformation of 5.8% under a transverse field of  $700 \text{ kA m}^{-1}$ . The material is first converted to a single field-preferred variant through the application of a high transverse field, and is subsequently compressed to a desired bias strain. The sample is then subjected to a sinusoidal transverse field of amplitude  $700 \text{ kA m}^{-1}$  and frequency of 0.25 Hz. A  $1 \times 2 \text{ mm}^2$  transverse Hall probe placed in the gap between a magnet pole and a face of the sample measures the flux density, from which the magnetization inside the material is obtained after accounting for demagnetization fields. The compressive force is measured by a 200 pounds of force (lbf) load cell, and the displacement is measured by a linear variable differential transducer. This process is repeated for several bias strains ranging between 1% and 5.5%.

Similar to the sensing model, the applied field ( $H$ ) and blocked bias strain ( $\epsilon_b$ ) constitute the independent variables, whereas the magnetization component in the  $x$  direction ( $M$ ) and stress ( $\sigma$ ) constitute the dependent variables. The overall model framework remains the same as in sensing model, with magnetic Gibbs energy as the primary thermodynamic potential. It is assumed that the volume fraction remains unchanged after initial compression during the field application because of the blocked configuration. The initial volume fraction before field application is calculated from the sensing model.



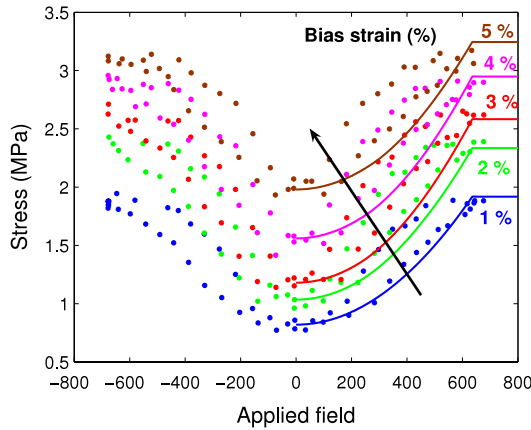


**Figure 18.** Stress–field at several blocked strains. Dots: experiment; solid line: model.

The magnetoelastic coupling is often ignored in the modeling of actuation and sensing in Ni–Mn–Ga, in which the strains due to variant reorientation are considerably larger than the magnetostrictive strains. This has been experimentally confirmed by Heczko [49] and Tickle *et al* [50]. The magnetoelastic energy is also ignored in the calculation of the magnetic parameters through expressions (37) and (38), as its contribution is around three orders of magnitude smaller than the other magnetic energy terms. However, the contribution of the magnetoelastic coupling to the generation of stress in mechanically blocked conditions is significant: twin boundary motion is completely suppressed and the magnetoelastic energy is the sole source of stress generation when a magnetic field is applied. The magnetoelastic energy is proposed to have the form

$$\rho\varphi_{me} = B_1\varepsilon_y(1 - \xi)(-\sin^2\theta) + \sigma_0\varepsilon_y\xi(-\sin^2\theta). \quad (67)$$

Here,  $B_1$  represents the magnetoelastic coupling coefficient [55] obtained by measuring the maximum stress generated when the sample is biased by 5.5% (when  $\xi = 0$ ), and  $\varepsilon_y$  represents the magnetostrictive strain in the  $y$  direction. The first term represents the magnetoelastic energy contribution due to magnetic fields, which contributes only in the stress-preferred variant ( $1 - \xi$ ). The second term represents the energy contribution due to the initial compressive stress  $\sigma_0$ . The applied field leads to an energy increase in stress-preferred variants, whereas the stress leads to an energy increase in the field-preferred variants. The stress generated due to magnetoelastic coupling thus has the form

$$\sigma_{me} = [B_1(1 - \xi) + \sigma_0\xi](-\sin^2\theta). \quad (68)$$

### 9.1. Results of blocked force behavior

Figure 18 shows experimental and calculated stress–applied field curves at several bias strains. Hysteresis is not included in the model. The significance of magnetoelastic coupling is evident as the stress starts increasing as soon as the field is applied and the magnetization vectors begin to rotate. The increase in stress is directly related to the angle of rotation

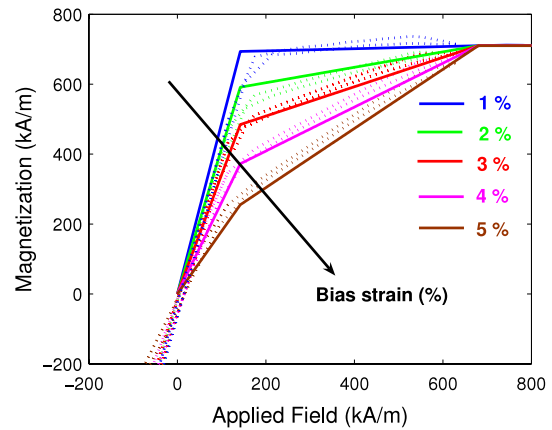


**Figure 19.** Magnetization–field at several blocked strains. Dashed line: experiment; solid line: model.

( $\theta$ ) predicted by the magnetization model. Conversely, the variant reorientation process is typically associated with a high amount of coercive field that increases with increasing bias stress [42, 7]. The absence of a coercive field, and of discontinuity in stress profiles, confirms the magnetoelastic coupling rather than twin reorientation as the origin of the stress.

Figure 19 shows the magnetization dependence on applied field at several blocked strains. The negligible hysteresis is typical of single crystal Ni–Mn–Ga when the volume fraction is approximately constant. Thus, the model assumption of reversible evolution of  $\alpha$  and  $\theta$  is validated along with the assumption of constant volume fraction. This is in contrast to figure 17, where the hysteresis occurs in concert with twin-variant rearrangement. The initial susceptibility of Ni–Mn–Ga varies significantly with bias strains, as the  $M$ – $H$  curve shifts between the two extreme cases of easy-axis and hard-axis curves. A 59% change in susceptibility is observed over a range of 4% change in strain. Figure 20 shows the variation of susceptibility with bias strain. The parameters employed for model calculations are:  $E_0 = 125$  MPa,  $E_1 = 2000$  MPa,  $\sigma_{tw0} = 1$  MPa,  $k = 16$  MPa,  $\varepsilon_0 = 0.055$ ,  $K_u = 2.2 \times 10^5$  J m $^{-3}$ ,  $M_s = 700$  kA m $^{-1}$ ,  $N = 0.2$ . Magnetoelastic coefficient  $B_1$  is the available blocking stress produced with 5.5% blocked strain, which is 1 MPa.

Our mechanically blocked measurements and thermodynamic model for constant volume fraction describe the stress and magnetization dependence on field, and provide a measure of the work capacity of Ni–Mn–Ga. The work capacity, defined as the area under the  $\sigma_{bl} - \sigma_0$  curve, is 72.4 kJ m $^{-3}$  for this material. This value compares favorably with that of Terfenol-D and PZT (18–73 kJ m $^{-3}$  [64]). However, the work capacity of Ni–Mn–Ga is strongly biased towards high deformations at the expense of low generated forces, which severely limits the actuation authority of the material. Terfenol-D exhibits a measured stress of 8.05 MPa at a field of 25 kA m $^{-1}$  and prestress of  $-6.9$  MPa [65]. The lower maximum available blocking stress of 1.47 MPa produced by Ni–Mn–Ga is attributed to a low magnetoelastic coupling.

The maximum available blocking stress is observed at a bias strain of 3%, though the maximum blocking stress occurs,

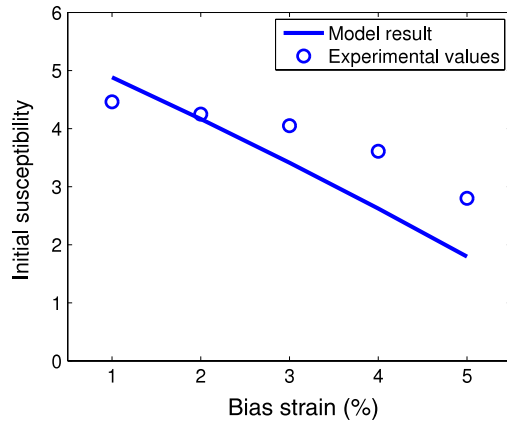


**Figure 20.** Variation of initial susceptibility with biased blocked strain.

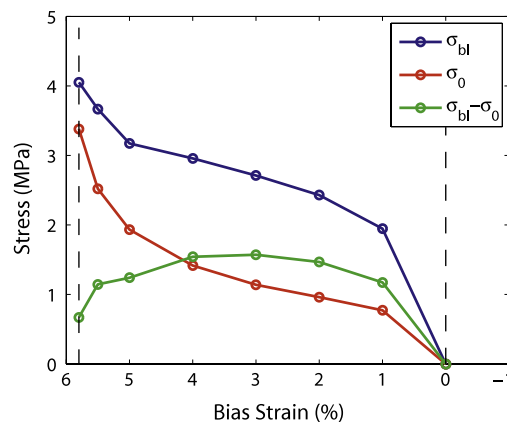


**Figure 21.** Experimental blocking stress  $\sigma_{bl}$ , minimum stress  $\sigma_0$ , and available blocking stress  $\sigma_{bl} - \sigma_0$  as a function of bias strain.

as expected, when the sample is completely prevented from deforming. Due to the competing effect of the stress-preferred and field-preferred variants, the stress is highest when the volume fractions are approximately equal ( $\xi = 0.5$ ) as seen in figure 21.

The magnetoelastic energy in Ni–Mn–Ga is considerably smaller than the Zeeman, magnetostatic, and anisotropy energies. The magnetostrictive strains in Ni–Mn–Ga are of the order of 50–300 ppm [49, 50], which are negligible when compared to the typical 6% deformation that occurs by twin-variant reorientation. The contribution of magnetoelastic coupling can thus be ignored when describing the sensing and actuation behavior in which the material deforms by several per cent strain. In the special case of field application in mechanically blocked conditions, twin-variant reorientation is completely suppressed and the magnetoelastic coupling becomes significant as it remains the only source of stress generation. This is validated from the experimental stress data as there is no coercive field associated with the twin-variant rearrangement. In summary, the magnetoelastic coupling in Ni–Mn–Ga is relatively low and becomes significant when the material is prevented from deforming.

## 10. Discussion

A unified magnetomechanical model based on the continuum thermodynamics approach is presented to describe the sensing [7], actuation [66] and blocked force [67] behavior of ferromagnetic shape memory Ni–Mn–Ga. The model requires only seven parameters, which are identified from two simple experiments: stress–strain plot at zero magnetic field, and easy-axis and hard-axis magnetization curves. The model parameter  $B_1$  is incorporated to describe the blocked force behavior. The model is low-order, with up to quadratic terms, which makes it convenient from the viewpoint of finite element implementation and incorporation in the structural dynamics of a system. The model spans three magnetomechanical characterization spaces, describing the interdependence of strain, stress, field and magnetization. The model accurately quantifies the dependent variables over large ranges of the bias independent variable, which is rarely seen in the literature. The magnetic Gibbs energy is the thermodynamic potential for sensing and blocked force models, whereas the Gibbs energy is the thermodynamic potential for the actuation effect.

Several important characteristics are investigated in concert with magnetomechanical characterization of single crystal Ni–Mn–Ga, along with the model predictions. The flux density sensitivity with strain ( $\frac{\partial B}{\partial \epsilon}$ ) varies from 0 to a maximum value of 4.19 T/% $\epsilon$  at a bias field of 173 kA m<sup>−1</sup>, and has a maximum reversible value of 2.38 T/% $\epsilon$  at a bias field of 368 kA m<sup>−1</sup> (figure 9). The stress induced by magnetic fields has a theoretical maximum value of 2.84 MPa (figure 7). The maximum field induced strain has a maximum reversible value of 5.8% at bias stresses of 0.89 and 1.16 MPa, which are optimum for actuation (figure 15). The initial susceptibility ( $\frac{\partial M}{\partial H}|_{H=0}$ ) changes by 59% over a range of 4% strain (figure 20) when the material is mechanically blocked. The maximum stress generation capacity is 1.47 MPa (over the bias stress) at 3% strain, which is 37% higher than that at the end values of blocked strain (figure 21). These parameters provide key insight into the magnetomechanical coupling of Ni–Mn–Ga.

Although the emphasis of the work is on a specific material single crystal Ni–Mn–Ga, the developed model can be applicable to any class of ferromagnetic shape memory materials. With recent advances in increased blocking stress [68], FSMA are a promising new class of multi-functional smart materials. Modeling polycrystalline behavior is one of the future opportunities which could be explored based on the results of this research. Possible future work could also involve extending the model framework for 3D cases which will enable design of structures that incorporate FSMA. Characterization in 3D involves the development of test setups capable of applying magnetic fields and mechanical loading in three directions simultaneously. The interference between these mechanisms presents a challenge which has not been addressed thus far. The modeling effort would require construction of energy terms that include magnetic fields in multiple directions, along with additional variants oriented with their long axis in the  $z$ -direction. Constitutive 3D models will also facilitate implementation of finite element analysis of structures to solve various magnetomechanical boundary value problems.

## Acknowledgments

This work was supported in part by the National Science Foundation under grant CMS-0409512, Dr Shih-Chi Liu, program director. We are grateful to the member organizations of the Smart Vehicle Concepts Center ([www.SmartVehicleCenter.org](http://www.SmartVehicleCenter.org)) and the National Science Foundation Industry/University Cooperative Research Centers program ([www.nsf.gov/eng/iip/iucrc](http://www.nsf.gov/eng/iip/iucrc)) for providing financial support. Additional support for NS was provided by the Smart Vehicle Concepts Center Fellowship Program.

## References

- [1] Murray S J, Marioni M, Allen S M, O'Handley R C and Lograsso T A 2000 6 percent magnetic-field-induced strain by twin-boundary motion in ferromagnetic Ni–Mn–Ga *Appl. Phys. Lett.* **77** 886–8
- [2] Henry C P, Bono D, Feuchtwanger J, Allen S M and O'Handley R C 2002 *J. Appl. Phys.* **91** 7810
- [3] Marioni M A, O'Handley R C and Allen S M 2003 Pulsed magnetic field-induced actuation of Ni–Mn–Ga single crystals *Appl. Phys. Lett.* **83** 3966–8
- [4] Soderberg O, Ge Y, Sozinov A, Hannula S and Lindroos V K 2005 Recent breakthrough development of the magnetic shape memory effect in Ni–Mn–Ga alloys *Smart Mater. Struct.* **14** S223–35
- [5] Kiang J and Tong L 2005 Modelling of magneto-mechanical behaviour of Ni–Mn–Ga single crystals *J. Magn. Magn. Mater.* **292** 394–412
- [6] Sarawate N and Dapino M 2006 Experimental characterization of the sensor effect in ferromagnetic shape memory Ni–Mn–Ga *Appl. Phys. Lett.* **88** 121923
- [7] Sarawate N and Dapino M 2007 A continuum thermodynamics model for the sensing effect in ferromagnetic shape memory Ni–Mn–Ga *J. Appl. Phys.* **101** 123522
- [8] O'Handley R C 1998 Model for strain and magnetization in magnetic shape-memory alloys *J. Appl. Phys.* **83** 3263–70
- [9] Likhachev A A and Ullakko K 2000 Quantitative model of large magnetostrain effect in ferromagnetic shape memory alloys *Eur. Phys. J. B* **14** 263–8
- [10] Hirsinger L and Lexcellent C 2003 Internal variable model for magneto-mechanical behavior of ferromagnetic shape memory alloys Ni–Mn–Ga *J. Physique IV* **112** 977–80
- [11] Jaaskelainen A, Aaltio I, Tellinen J, Suorsa I and Ullakko K 2002 Basic properties of magnetic shape memory actuator *8th Int. Conf. on ACTUATOR2002 (Bremen, June 2002)* pp 566–9
- [12] James R and Wuttig M 2004 Magnetostriction of martensite *Phil. Mag.* **77** 1273–99
- [13] DeSimone A and James R D 1997 A theory of magnetostriction oriented towards applications *J. Appl. Phys.* **81** 5706–8
- [14] DeSimone A and James R D 1997 A constrained theory of magnetoelasticity *J. Mech. Phys. Solids* **50** 283–320
- [15] Tickle R, James R D, Shield T, Wuttig M and Kokorin V V 1999 Ferromagnetic shape memory in the Ni–Mn–Ga system *IEEE Trans. Magn.* **35** 4301–10
- [16] James R D, Tickle R and Wuttig M 1999 Large field-induced strains in ferromagnetic shape memory materials *J. Magn. Magn. Mater.* **273–295** 320–5
- [17] Likhachev A A and Ullakko K 2000 Magnetic-field-controlled twin boundaries motion and giant magneto-mechanical effects in Ni–Mn–Ga shape memory alloy *Phys. Lett. A* **275** 142–51
- [18] Likhachev A A and Ullakko K 2001 The model development and experimental investigation of giant magneto-mechanical effects in Ni–Mn–Ga *J. Magn. Magn. Mater.* **226–230** 1541–3
- [19] Likhachev A A, Sozinov A and Ullakko K 2002 Optimizing work output in Ni–Mn–Ga and other ferromagnetic shape memory alloys *Proc. SPIE Smart Structures and Materials* vol 4699, pp 553–63
- [20] Likhachev A A, Sozinov A and Ullakko K 2003 Magnetic shape memory—mechanism, modeling principles and their application to Ni–Mn–Ga *J. Physique IV* **112** 981–4
- [21] Likhachev A A, Sozinov A and Ullakko K 2004 Different modeling concepts of magnetic shape memory and their comparison with some experimental results obtained in Ni–Mn–Ga *Mater. Sci. Eng. A* **378** 513–8
- [22] Likhachev A A, Sozinov A and Ullakko K 2006 Modeling the strain response, magneto-mechanical cycling under the external stress, work output and energy losses in Ni–Mn–Ga *Mech. Mater.* **38** 551–63
- [23] Straka L and Heczko O 2006 Magnetization changes in Ni–Mn–Ga magnetic shape memory single crystal during compressive stress reorientation *Scr. Mater.* **54** 1549–52
- [24] Heczko O 2005 Magnetic shape memory effect and magnetization reversal *J. Magn. Magn. Mater.* **290/291** 787–94
- [25] Heczko O, L'vov V A, Straka L and Hannula S P 2006 Magnetic indication of the stress-induced martensitic transformation in ferromagnetic Ni–Mn–Ga alloy *J. Magn. Magn. Mater.* **302** 387–90
- [26] Murray S J, O'Handley R C and Allen S M 2001 Model for discontinuous actuation of ferromagnetic shape memory alloy under stress *J. Appl. Phys.* **89** 1295–301
- [27] O'Handley R C, Murray S J, Marioni M, Nembach H and Allen S M 2000 Phenomenology of giant magnetic-field-induced strain in ferromagnetic shape-memory materials (invited) *J. Appl. Phys.* **87** 4712–7
- [28] O'Handley R C, Paul D I, Marioni M, Henry C P, Richard M, Tello P G and Allen S M 2003 Micromagnetics and micromechanics of Ni–Mn–Ga actuation *J. Physique IV* **112** 972–6
- [29] Couch R N and Chopra I 2005 Quasi-static modeling of Ni–Mn–Ga magnetic shape memory alloy *Proc. SPIE Smart Structures and Materials (San Diego, CA, March 2005)* vol 5764, pp 1–12
- [30] Couch R N and Chopra I 2007 A quasi-static model for Ni–Mn–Ga magnetic shape memory alloy *Smart Mater. Struct.* **16** S11–21
- [31] Couch R N, Sirohi J and Chopra I 2007 Development of a quasi-static model of Ni–Mn–Ga magnetic shape memory alloy *J. Intell. Mater. Syst. Struct.* **18** 611–20
- [32] Brinson L C 1993 One-dimensional constitutive behavior of shape memory alloys: thermo-mechanical derivation with non-constant material functions *J. Intell. Mater. Syst. Struct.* **4** 229–42
- [33] Brinson L C and Huang M S 1995 Simplifications and comparisons of shape memory alloy constitutive models *J. Intell. Mater. Syst. Struct.* **7** 108–14
- [34] Glavatska N I, Rudenko A A, Glavatskiy I N and L'vov V A 2003 Statistical model of magnetostrain effect in martensite *J. Magn. Magn. Mater.* **265** 142–51
- [35] Chernenko V A, L'vov V A, Mullner P, Kistorz G and Takagi T 2004 Magnetic-field-induced superelasticity of ferromagnetic thermoelastic martensites: experiment and modeling *Phys. Rev. B* **69** 134410
- [36] Chernenko V A, L'vov V A, Cesari E, Pons J, Rudenko A A, Date H, Matsumoto M and Kanomata T 2004 Stress-strain behaviour of Ni–Mn–Ga alloys: experiment and modelling *Mater. Sci. Eng. A* **378** 349–52
- [37] Hirsinger L and Lexcellent C 2003 Modelling detwinning of martensite platelets under magnetic and (or) stress actions on Ni–Mn–Ga alloys *J. Magn. Magn. Mater.* **254/255** 275–7



- [38] Hirsinger L 2004 Modelling of magneto-mechanical hysteresis loops in Ni–Mn–Ga shape memory alloys *Phys. Status Solidi c* **1** 3458–62
- [39] Hirsinger L 2004 Ni–Mn–Ga shape memory alloys: modelling of magneto-mechanical behaviour *Int. J. Appl. Electromagn. Mech.* **19** 473–7
- [40] Creton N and Hirsinger L 2005 Rearrangement surfaces under magnetic field and/or stress in Ni–Mn–Ga *J. Magn. Magn. Mater.* **290/291** 832–5
- [41] Gauthier J Y, Lexcelent C, Hubert A, Abadie J and Chaillet N 2007 Modeling rearrangement process of martensite platelets in a magnetic shape memory alloy Ni<sub>2</sub>MnGa single crystal under magnetic field and (or) stress action *J. Intell. Mater. Syst. Struct.* **18** 289–99
- [42] Kiefer B and Lagoudas D C 2005 Magnetic field-induced martensitic variant reorientation in magnetic shape memory alloys *Phil. Mag.* **85** 4289–329
- [43] Kiefer B and Lagoudas D C 2005 Modeling of the magnetic field-induced martensitic variant reorientation and the associated magnetic shape memory effect in MSMAs *Proc. SPIE Smart Structures and Materials (San Diego, CA, March 2005)* vol 5761, pp 454–65
- [44] Kiefer B, Karaca H E, Lagoudas D C and Karaman I 2007 Characterization and modeling of the magnetic field-induced strain and work output in Ni<sub>2</sub>MnGa magnetic shape memory alloys *J. Magn. Magn. Mater.* **312** 164–75
- [45] Faidley L E, Dapino M J, Washington G N and Lograsso T A 2005 Reversible strain in Ni–Mn–Ga with collinear field and stress *Proc. SPIE Smart Structures and Materials (San Diego, CA, March 2005)* vol 5761, pp 501–12
- [46] Faidley L E, Dapino M J, Washington G N and Lograsso T A 2006 Modulus increase with magnetic field in ferromagnetic shape memory Ni–Mn–Ga *J. Intell. Mater. Syst. Struct.* **17** 123–31
- [47] Faidley L E, Dapino M J and Washington G N 2008 Homogenized strain model for Ni–Mn–Ga driven with collinear magnetic field and stress *J. Intell. Mater. Syst. Struct.* **19** 681–94
- [48] Malla A, Dapino M, Lograsso T A and Schlagel D L 2006 Large magnetically induced strains in Ni<sub>50</sub>Mn<sub>28.7</sub>Ga<sub>21.3</sub> driven with collinear field and stress *J. Appl. Phys.* **99** 063903
- [49] Heczko O 2005 Determination of ordinary magnetostriction in Ni–Mn–Ga magnetic shape memory alloy *J. Magn. Magn. Mater.* **290/291** 846–9
- [50] Tickle R and James R D 1999 Magnetic and magnetomechanical properties of Ni<sub>2</sub>MnGa *J. Magn. Magn. Mater.* **195** 627–38
- [51] Murray S, Allen S M, O’Handley R C and Lograsso T 2000 Magneto-mechanical performance and mechanical properties of Ni–Mn–Ga ferromagnetic shape memory alloys *Proc. SPIE Smart Structures and Materials (San Diego, CA, March 2000)* vol 3992, pp 387–95
- [52] Pao Y H and Hutter K 1975 Electrodynamics for moving elastic solids and viscous fluids *Proc. IEEE* **63** 1011–21
- [53] Coleman B D and Gurtin M E 1967 Thermodynamics with internal state variables *J. Chem. Phys.* **47** 597–613
- [54] Ge Y, Heczko O, Soderberg O and Lindroos V K 2004 Various magnetic domain structures in a Ni–Mn–Ga martensite exhibiting magnetic shape memory effect *J. Appl. Phys.* **96** 2159–63
- [55] O’Handley R C 2000 *Modern Magnetic Materials: Principles and Applications* (New York: Wiley)
- [56] Boyd J G and Lagoudas D C 1996 A thermodynamical constitutive model for shape memory materials. Part I. The monolithic shape memory alloy *Int. J. Plast.* **12** 805–42
- [57] Bo Z and Lagoudas D C 1999 Thermomechanical modeling of polycrystalline SMAs under cyclic loading, part I: theoretical derivations *Int. J. Eng. Sci.* **37** 1089–140
- [58] Jiles D C 1991 *Introduction to Magnetism and Magnetic Materials* (London: Chapman and Hall)
- [59] Henry C P 2002 Dynamic actuation response of Ni–Mn–Ga ferromagnetic shape memory alloys *PhD Thesis* Massachusetts Institute of Technology
- [60] Jaaskelainen A, Ullakko K and Lindroos V K 2003 Magnetic field-induced strain and stress in a Ni–Mn–Ga alloy *J. Physique IV* **112** 1005–8
- [61] Couch R N and Chopra I 2006 Testing and modeling of Ni–Mn–Ga ferromagnetic shape memory alloy for static and dynamic loading conditions *Proc. SPIE Smart Structures and Materials (San Diego, CA, March 2006)* vol 6173, pp 501–16
- [62] Ma Y F and Li J Y 2007 Magnetization rotation and rearrangement of martensite variants in ferromagnetic shape memory alloys *Appl. Phys. Lett.* **90** 172504
- [63] Landis C M 2008 A continuum thermodynamics formulation for micro-magnetomechanics with applications to ferromagnetic shape memory alloys *J. Mech. Phys. Solids* **56** 3059–76
- [64] Giurgiutiu V, Rogers C A and Chaudhry Z 1996 Energy-based comparison of solid-state induced-strain actuators *J. Intell. Mater. Syst. Struct.* **7** 4–14
- [65] Dapino M J, Smith R C, Faidley L E and Flatau A B 2000 A coupled structural-magnetic strain and stress model for magnetostrictive transducers *J. Intell. Mater. Syst. Struct.* **11** 135–52
- [66] Sarawate N and Dapino M 2007 Magnetomechanical characterization and unified actuator/sensor modeling of ferromagnetic shape memory alloy Ni–Mn–Ga *Proc. SPIE Smart Structures and Materials (San Diego, CA, March 2007)* vol 6526, p 652629
- [67] Sarawate N and Dapino M 2008 Magnetic-field-induced stress and magnetization in mechanically blocked Ni–Mn–Ga *J. Appl. Phys.* **103** 083902
- [68] Karaca H E, Karaman I, Basaran B, Chumlyakov Y I and Maier H J 2006 Magnetic field and stress induced martensite reorientation in Ni–Mn–Ga ferromagnetic shape memory alloy single crystals *Acta Mater.* **54** 233–45